frontiers | Frontiers in Earth Science

TYPE Original Research
PUBLISHED 21 December 2022
DOI 10.3389/feart.2022.1021550

Check for updates

OPEN ACCESS

EDITED BY
Maoliang Zhang,
Tianjin University, China

REVIEWED BY
Peiyue Li,
Chang'an University, China
Yong Xiao,
Southwest Jiaotong University, China

*CORRESPONDENCE
Xiaocheng Zhou,
zhouxiaocheng188@163.com
Yang Li,
liyangxbdx@163.com

SPECIALTY SECTION
This article was submitted to Geochemistry, a section of the journal Frontiers in Earth Science

RECEIVED 17 August 2022
ACCEPTED 07 November 2022
PUBLISHED 21 December 2022

CITATION
Wang J, Zhou X, He M, Li J, Dong J, Tian J, Yan Y, Li Y, Liu K and Li Y (2022), Hydrogeochemical origin and circulation of spring waters along the Karakorum fault, Western Tibetan Plateau: Implications for interaction between hydrosphere and lithosphere. *Front. Earth Sci.* 10:1021550. doi: 10.3389/feart.2022.1021550

COPYRIGHT
© 2022 Wang, Zhou, He, Li, Dong, Tian, Yan, Li, Liu and Li. This is an open-access article distributed under the terms of the Creative Commons Attribution License (CC BY). The use, distribution or reproduction in other forums is permitted, provided the original author(s) and the copyright owner(s) are credited and that the original publication in this journal is cited, in accordance with accepted academic practice. No use, distribution or reproduction is permitted which does not comply with these terms.

Hydrogeochemical origin and circulation of spring waters along the Karakorum fault, Western Tibetan Plateau: Implications for interaction between hydrosphere and lithosphere

Jingli Wang[1,2], Xiaocheng Zhou[3]*, Miao He[3], Jingchao Li[3], Jinyuan Dong[3], Jiao Tian[3], Yucong Yan[3], Ying Li[3], Kaiyi Liu[4] and Yang Li[1]*

[1]State Key Laboratory of Continental Dynamics, Department of Geology, Northwest University, Xi'an, China, [2]School of Petroleum Engineering and Environmental Engineering, Yan'an University, Yan'an, China, [3]United Laboratory of High-Pressure Physics and Earthquake Science, Institute of Earthquake Forecasting, CEA, Beijing, China, [4]The University of Sydney Business School, University of Sydney, Sydney, NSW, Australia

Geochemical investigation on the origin and circulation of geothermal water is crucial for better understanding the interaction between hydrosphere and lithosphere. Previous studies on the Himalayan geothermal belt mainly distributed in the central and eastern Tibetan Plateau. In this study, water samples (8 hot springs and 1 cold spring) from the Karakorum fault (KKF) zone of western Tibetan Plateau were analyzed for the hydrogeochemical characteristics and isotopic compositions. Three types of spring water along the KKF were classified on basis of ionic concentration and Sr isotopic composition: type A water (HCO_3–Mg or Ca), type B water (HCO_3–Na) and type C water (Cl–Na). Type A water is originated from the infiltration of meteoric water and the dissolution of silicate/evaporite. Type B water is mainly leached from the metamorphic and granitoid rocks. Type C water is formed by the dissolution of chlorides and sulphates. δD and $\delta^{18}O$ isotopes indicate that geothermal fluid along the fault zone was mainly recharged by local precipitation. Moreover, reservoir temperatures of 144.2–208.6°C were estimated by the silica–enthalpy mixing model, and the thermal waters have a relatively deep circulation depth (≥ 7.0 km). Meanwhile, the thermal waters are characterized by extremely high Li, B, Fe and As concentrations and earthquakes frequently happened in the vicinity, suggesting that the KKF is a deep and active fault, which also indicates that the thermal fluids are strongly associated with seismicity. Therefore, thermal fluid can potentially be used as continuous monitoring sites for earthquake forecasting.

KEYWORDS

hydrogeochemistry, water-rock interaction, circulation model, spring along Karakorum fault, western Tibetan Plateau

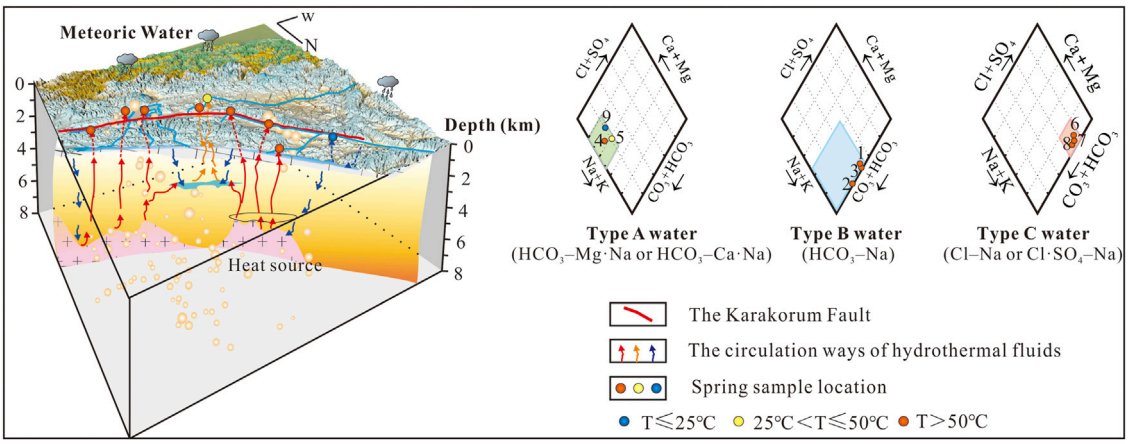

GRAPHICAL ABSTRACT

1 Introduction

Geothermal energy is one of the most competitive resources with the potential to substitute fossil fuels in the future (Wang, 2009; Vakulchuk et al., 2020). Hot spring water, a geothermal resource that develops mostly along faults, acts as a window of deeper and shallower crusts, and is closely related to deep thermal systems (Bianchi et al., 2010; Guo, 2012). The geochemical characterisation of geothermal water not only contributes to the exploration and development of geothermal resources but also provides information about the geothermal reservoirs (Guo et al., 2014a, b; Brahim et al., 2020), the tectonic setting, activity and penetration depth of related faults (Du et al., 2005; Zhao et al., 2014; Daniele et al., 2020). New findings have been made in understanding the genesis type, recharge source, reservoir temperature, circulation depth and formation mechanisms of geothermal water and even some earthquake precursor signals (Skelton et al., 2019; Barberio et al., 2020; Franchini et al., 2021; Yan et al., 2022). In addition, geothermal water is one of the important windows to study the interaction between the lithosphere and hydrosphere.

The India-Eurasia continental collision, ongoing since ca. 60–50 Ma (Molnar and Tapponnier, 1975; Hu et al., 2015; Zhu et al., 2021), has created the Tibetan Plateau. Many medium- to high-temperature geothermal resources have developed in the Tibetan Plateau (Figure 1A) located in the Himalayas geothermal belt, which is an important part of the Mediterranean–Himalayas geothermal belt (Guo, 2012) and provides ideal systems for studying the deep-time interaction between the lithosphere and hydrosphere. Systematic geological works, including geochemical investigations and quantitative assessment of the geothermal reservoirs, have been conducted in the central and eastern Tibetan Plateau, such as the Yangyi geothermal system (The Geothermal Geological Team of Tibet, 1990; Guo et al., 2009; Yuan et al., 2014), the Rehai geothermal system (Shangguan and Huo, 2002; Guo et al., 2014a, b), the Yangbajing geothermal system (Guo et al., 2008, 2010; Yuan et al., 2014) and the Kangding–Litang–Batang geothermal belt (Tang et al., 2017). Moreover, it has been verified that the magma chamber or molten granite is the heat source for most of these high-temperature (> 150°C) hydrothermal systems (Nelson et al., 1996; Guo and Wang, 2012). However, due to location approaching the disputed international boundaries at a high elevation, relatively few systematic studies have been conducted on the high-temperature geothermal fields with non-volcanogenic heat sources in the western Tibetan Plateau (Wu et al., 2011; He et al., 2016; Wang et al., 2016).

In this contribution, the interaction of deep lithosphere and hydrosphere was discussed by the study of thermal and cold springs along the Karakorum fault (KKF) in the western Tibetan Plateau. Systematical analyses, including physicochemical characteristics (including pH and electrical conductivity), hydrochemical characteristics (anion, cation and trace element concentrations), stable hydrogen and oxygen isotopic compositions and Sr isotopic compositions, were conducted to construct a model of the origin and circulation for the geothermal water. The petrological characteristics and penetration depth of the KKF were also analyzed to identify whether high-temperature geothermal fluids in the study area were heated by magma or other heat source. About the geochemical study of spring waters along the KKF, it can be used to estimate the circulation depth of geothermal fluids that have closed relationships to earthquake distribution. So we speculate that geothermal fluids can be considered as potential continuous monitoring sites for forecasting shallow-focus earthquakes and compensating for the shortcomings of conventional fluid seismic observations in the future.

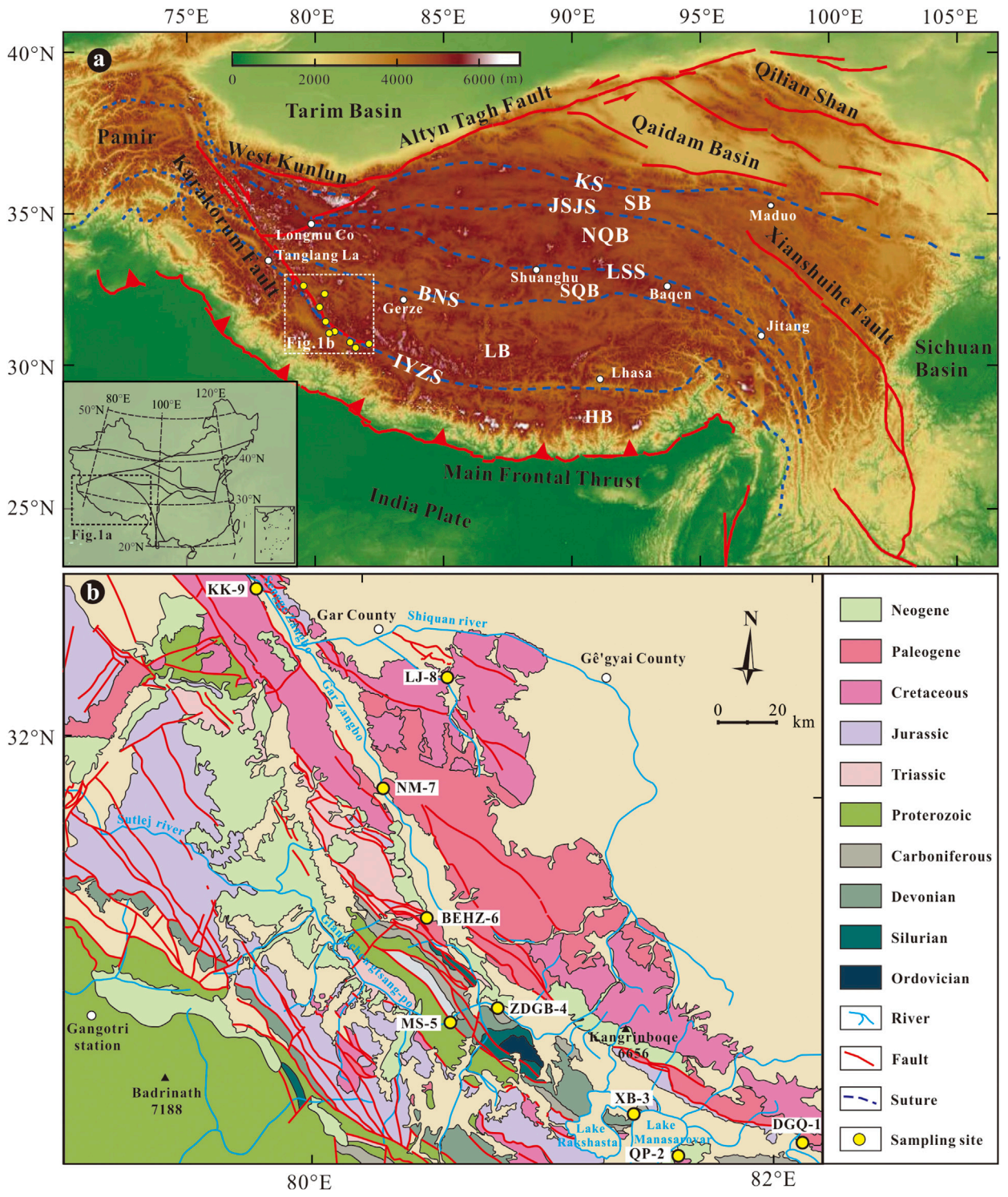

FIGURE 1
(A) Tectonic framework of the Tibet and surrounding regions (modified after Lu et al., 2022); **(B)** Geological map with sampling sites of the study area. Abbreviations: HB- Himalayan block; LB- Lhasa block; SQB- South Qiangtang block; NQB- North Qiangtang block; SB- Songpan-Ganze block; KS- Kunlun suture; JSJS- Jinshajiang suture; LSS- Longmu Co-Shuanghu suture; BNS- Bangong Co-Nujiang suture; IYZS- India-Yarlung Zangbo suture.

2 Hydrogeologic and geological setting

The KKF is characterised by a highland monsoon climate, with an elevation range of 4,200–4,900 m, average annual temperature of 0.4°C and average annual precipitation of 74.8 mm/yr (Wu et al., 2011). The annual solar radiation in the town of Shiquanhe is as high as 8.16×10^{15} J/m^2, which is the highest value in Tibet. Geologically, the KKF is a dextral strike–slip active fault that trends NW–SE, stretching for more than 1,000 km from the Pamir to the Indus–Tsangpo suture zone. South of Shiquanhe, the southeastern segment of the KKF extends along the Indus–Tsangpo suture zone eastward of the Kailas range for at least 150 km and becomes parallel to the Indus suture (Lacassin et al., 2004). Its contemporary and late Pleistocene slip rates are in dispute [InSAR: 1 ± 3 mm/yr (Wright et al., 2004); GPS: ≈3–5 mm/yr (Kundu et al., 2014; Z. Tian et al., 2019); ≈11 mm/yr (Banerjee and Bürgmann, 2002)]. Although investigations on the penetration depth of the KKF have been carried out (Rai et al., 2006; Priestley et al., 2008; Nábělek et al., 2009; Zhao et al., 2010; Klemperer et al., 2013; He et al., 2016), whether the KKF access to the mantle depth remain unclear.

Strata that outcrop in the KKF area are mainly covered by sediments, including Holocene (Qh^{alp}), Pleistocene (Qp), Paleogene (N_2w), Oligocene to early Miocene (E_3N_1r) and Middle Cretaceous (K_2s) that consist of carbonate breccia, calcareous sinter, gravels, sandstones, mudstones and shales. In addition, Magmatic rocks in the study area mainly contain Upper Cretaceous granodiorite ($K_2\gamma\delta$), the Lower Cretaceous (K_1d and K_1l), the Upper Triassic mafic rocks ($T_3M\sum$) and complex rocks ($T_3M\sum m$), the Lower Neocene monzogranite ($\eta\gamma N_1$). Overall, the most widespread strata in the KKF are Cretaceous. Lower Cretaceous shallow marine and terrestrial deposits intruded by Gangdese granitoids with predominantly Cretaceous and rarely Cenozoic ages (Schwab et al., 2004), unconformably overlie ophiolitic mélange and locally Permian metasediments (Kapp et al., 2003). Strong Cretaceous and Cenozoic magmatism and metamorphism of the KKF, which are related to an Andean-type margin along the southern margin of Asia (Schwab et al., 2004), offer the required conditions for the development of abundant large-scale geothermal resources along the KKF. The fault provides channels for the circulation of geothermal fluids (Sachan et al., 2016), facilitating water–rock interaction and convection of heat (Wang et al., 2016).

Some previous studies have depended on geological and geophysical data to examine geothermal water along the KKF. However, a few geochemical investigations on the hydrothermal waters of the KKF field have been conducted and examined the ion origin and phase equilibrium of minerals, the mixing of thermal and cold waters, and the geothermal reservoir temperature (e.g., Wu et al., 2011; Wang et al., 2016). No works have been reported about the circulation depth and circulation models of the geothermal water along the KKF.

3 Methodology

3.1 Sampling and analytical procedures

A total of nine samples were obtained from eight thermal springs (DGQ-1, QP-2, XB-3, ZDGB-4, MS-5, BEHZ-6, NM-7, LJ-8) and the Kalakoram cold spring (KK-9), distributing along the KKF of the western Tibetan Plateau Figure 1B. The samples were collected for chemical and isotope analyses on August 2–4, 2019, except for the sample from the Kalakunlun Mountain spring, which was collected on 8 October 2020, and the sample from sample ZDGB-4, which was collected on 28 September 2021. The longitude, latitude, elevation, lithology, and aquifer type of each sampling site were recorded during the sampling. The physicochemical parameters of the thermal water samples, including pH and electrical conductivity (EC), were measured on site using a Thermo Orion 4-Star Meter, which was calibrated before sampling. The water temperature was determined using a YF-160 thermometer, and the measurement error was estimated to be within 0.1°C. The water samples were collected by underwater sampling and were stored in 50-mL polyethene (PE) bottles that had been pre-cleaned by immersion in ultrapure water for 3 days, oscillation in an ultrasonic oscillator for 15 min, rinsing in ultrapure water and drying in an oven. One vial was an unacidified sample used for anion analyses, and another vial was acidified with analytical reagent (AR) for cation and trace element analyses.

Chemical analysis of the spring water samples was performed in the Key Laboratory of the Earthquake Forecasting Institute of the China Earthquake Administration. The concentrations of cations (K^+, Na^+, Mg^{2+}, Ca^{2+}, Li^+) and anions (F^-, Cl^-, NO_3^- and SO_4^{2-}) in the water samples were determined using an ion chromatography system (Dionex ICS-900) and an autosampler (AS40) with a detection limit of 0.01 mg/L (Chen et al., 2015). The HCO_3^- and CO_3^{2-} concentrations of the samples were measured with a ZDJ-3D titrator with 0.05 mol/L HCl, using methyl orange and phenolphthalein indicators. For the purpose of calibration of the chromatography, the standard samples were measured before and after measurement of each batch of water samples. The deviation of the measurements was within ± 1%.

The concentrations of trace elements were detected by inductively coupled plasma mass spectrometry (ICP-MS, Element XR) in the Analytical Laboratory of the Beijing Research Institute of Uranium Geology (Knappett et al., 2018). Sr isotope compositions were determined using a thermoionisation mass spectrometer (TIMS, IsotopX Phenix), largely according to the experimental procedures described by Wang et al. (2014). Silica (SiO_2) concentrations were analysed using an inductively coupled plasma optical emission spectrometer (ICP-OES) (Perkin-Elmer Optima 5300DV, United States). The O and H isotopic compositions of the water samples were

determined using a Thermo-Finnigan MAT253 mass spectrometer. The O–H isotopic results are reported in delta (δ) notation *versus* the international Vienna Standard Mean Ocean Water (VSMOW) and expressed in per-mile percentages. The precisions were better than ± 0.2‰ and ± 1‰ for $\delta^{18}O$ and δD, respectively (Liu et al., 2013).

3.2 Hydrochemistry and isotopes

The spring waters were classified according to the Schukarev classification system. The total equivalents of cations and anions were taken to be 100%, and ions greater than 25% of the milligram equivalents were considered in the classification. Piper (1944) proposed an effective tool (Piper diagram) based on a multiple-trilinear diagram with respect to sources of hydrochemical constituents and water–rock interaction processe. A $Cl–SO_4–HCO_3$ ternary diagram was used to determine whether there is a volatile magmatic influence on the high-temperature geothermal fluid (Giggenbach, 1988). The triangular Na–K–Mg diagram can be used to evaluate the equilibrium between hot water and rocks, which can further distinguish three states of water: fully equilibrated water, partially equilibrated (mixed) water and immature water.

Stable oxygen and hydrogen isotopes can be used to calculate the recharge elevation of meteoric waters because of their relationship with altitude (Craig, 1961), and to trace the origin of hydrothermal waters (Giggenbach et al., 1983). Studies of the δD and $\delta^{18}O$ values of precipitation related to altitude (Craig, 1961) suggest that the isotopes of meteoric water become progressively lighter with increasing altitude. Thus, the recharge elevation of groundwater can be estimated by using the following formula:

$$H = \frac{\delta^{18}O_{gw} - \delta^{18}O_{lw}}{\mathrm{grad}^{18}O} + h$$

where H (m) is the recharge elevation; $\delta^{18}O_{gw}$ and $\delta^{18}O_{lw}$ (‰) are the oxygen isotope ratios of the groundwater sample and local meteoric water, respectively; $\mathrm{grad}^{18}O$ (‰/km) is the isotope elevation gradient of meteoric water; and h (m) is the elevation of the local meteoric water sampling point.

The mixing ratio of magmatic water in geothermal fluid can be calculated using the following isotopic bivariate mixture model (Pang, 2006):

$$\delta_G = \lambda\delta_M + (1-\lambda)\delta_P$$

where δ_G, δ_M, and δ_P represent the $\delta^{18}O$ or δD of geothermal fluid, magmatic water and precipitated meteoric water, respectively. λ is the percentage of magmatic water mixed in the geothermal fluid.

Strontium isotope ratios are originally used as a geochronologic tool and a petrogenetic tracer to determine the age or source of rock formations (Faure, 1977), since rocks or minerals have different ages and Rb/Sr ratios, resulting in variable strontium isotopes in different geological terranes (Hajj et al., 2017). Later, strontium isotopes have been used to investigate Earth surface processes, such as quantifying the weathering and erosion rates of rocks and calculating the contributions of different mixing sources to water bodies (Gaillardet et al., 1999; Wang and Tang, 2020) Strontium in rocks is released into water and soil as Sr primarily through weathering and dissolution. The $^{87}Sr/^{86}Sr$ values of surface and ground water are a function of bedrock weathering (Frei and Frei, 2011). Previous studies have concluded that the dominant source of Sr (water, plants, soils, snail shells and animal and human tooth enamel and bones) is largely determined by the underlying geology (Hajj et al., 2017).

3.3 Statistical analysis and geochemical modeling

As the Lower Cretaceous shallow marine and terrestrial deposits were intruded by the Gangdese granitoid (Schwab et al., 2004), the geothermal water in the KKF area likely interacted with the intruding granite. So, the corresponding trace element compositions of granodiorite from Jiangba pluton in the Shiquanhe area (Yan, 2019) were used as the reference. Ti was selected as the reference element because of its widespread presence in the crust, low susceptibility to contamination, stable chemical properties and lower volatility than other trace elements. In this study, the enrichment factor (EF), a qualitative indicator used to assess the water–rock interaction of thermal waters, was calculated by normalizing the concentrations of trace elements (Li, Be, Al, Ti, V, Cr, Fe, Co, Ni, Cu, Zn, Sr, Sn, Ba, Tl, Pb, Th and U) using the following formula:

$$EF_i = \frac{(C_i/T_i)_\omega}{(C_i/T_i)_r}$$

where T_i is the selected reference element, C_i is an element in the spring sample, ω is the element concentration of the spring sample, and r is the element concentration of the reference rocks.

The AquaChem–PHREEQC software (Parkhurst and Appelo, 1999) developed by Waterloo Hydrogeologic Inc. was used to evaluate the geochemical properties and saturation index of each mineral.

The silica–enthalpy mixing model is another available method for determining reservoir temperatures of spring water. The silica–enthalpy mixing model (Fournier and Truesdell, 1974) assumes that 1) there is no precipitation of silicon and SiO_2 controlled by quartz in thermal water before mixing with cold water; 2) and no conduction cooling occurs after mixing. These factors eliminate the effects of the mixing process and represent the maximum reservoir temperatures of thermal water before mixing. In this study, sample KK-9 is selected as the end-member of cold water, while the other

TABLE 1 Hydrochemical properties and major chemical constituents of the spring waters along the Karakorum Fault. The values were expressed in mg/L.

Sample	Type of sample	T (°C)	pH	EC (μs/cm)	Na	K	Mg	Ca	Cl	SO_4	CO_3	HCO_3	Li	F	SiO_2	TDS	Hydrochemical type	δD (‰)	$\delta^{18}O$ (‰)
DGQ-1	Geothermal spring	75.00	7.75	45600	770.67	78.90	10.80	20.90	742.48	57.76	87.94	1299.28	16.16	11.19	81.11	1230.04	HCO_3·Cl–Na	−142.7	−16.4
QP-2	Geothermal spring	83.40	8.28	1697	367.97	32.44	0.87	4.05	112.63	86.43	98.58	498.22	2.41	11.87	214.00	679.49	HCO_3–Na	−136.3	−16.8
XB-3	Geothermal spring	70.00	8.11	47000	1005.71	97.48	3.00	14.34	676.75	257.83	160.28	1360.56	9.50	6.81	149.59	1694.18	HCO_3·Cl–Na	−121.8	−15.3
ZDGB-4	Geothermal spring	69.60	7.29	144.7	118.09	38.42	38.94	148.78	15.05	85.49	0.00	852.78	0.34	3.19	46.87	60.28	HCO_3–Ca·Na	−128.4	−15.5
MS-5	Geothermal spring	48.50	6.72	2412	225.44	98.57	177.65	50.25	67.21	181.75	0.00	1307.21	0.68	1.44	32.96	176.00	HCO_3–Mg·Na	−130.4	−16.5
BEHZ-6	Geothermal spring	74.00	7.87	62900	1082.17	135.49	21.65	59.11	1822.34	137.11	145.39	845.04	36.88	8.14	153.44	3196.92	Cl–Na	−115.8	−13.3
NM-7	Geothermal spring	77.88	8.10	1245	250.92	8.84	0.21	11.51	179.87	145.00	28.37	135.55	0.96	15.08	77.25	649.49	Cl·SO_4–Na	−131.4	−14.3
LJ-8	Geothermal spring	81.17	8.20	2813	573.14	43.65	1.93	24.80	444.78	374.87	73.76	440.54	5.56	10.01	147.45	1478.20	Cl·SO_4–Na	−119.9	−13.3
KK-9	Cold spring	6.00	7.43	155.10	11.33	0.88	3.81	18.00	1.40	14.54	0.00	79.52	0.00	0.77	8.65	20.66	HCO_3–Ca·Na	−124.7	−15.5

Note: δD and $\delta^{18}O$ were expressed in ‰ vs. V-SMOW, standard.

10.3389/feart.2022.1021550

TABLE 2 Chemical composition of trace elements of the spring waters along the Karakorum Fault. The values were expressed in μg/L.

Sample	DGQ-1	QP-2	XB-3	ZDGB-4	MS-5	BEHZ-6	NM-7	LJ-8	KK-9
Li	16935.00	2251.00	9235.00	320.00	627.00	35553.00	923.00	5091.00	12.80
Be	26.90	5.91	2.10	0.27	0.09	14.10	1.48	4.35	0.08
B	315473.00	40509.00	84849.00	3004.00	10351.00	497014.00	19451.00	52286.00	326.00
Al	70.60	486.00	168.00	8.46	9.10	69.00	96.20	33.40	265.00
Ti	20.50	31.70	29.90	5.14	8.27	32.70	9.38	22.00	23.80
V	3.72	1.16	3.18	2.15	0.96	6.64	1.28	2.25	2.12
Cr	2.07	2.77	2.68	2.52	1.58	1.72	1.56	1.69	2.60
Fe	344.00	259.00	331.00	85.30	12.80	411.00	90.50	97.00	568.00
Co	0.06	0.10	0.16	0.47	0.31	0.09	0.06	0.05	0.31
Ni	0.92	1.20	1.35	7.39	3.65	1.51	0.75	0.65	1.62
Cu	1.42	1.35	2.35	1.82	1.84	1.72	1.19	2.64	31.70
Zn	4.80	3.99	5.02	12.10	5.11	5.58	3.14	4.69	17.00
Sr	1465.00	216.00	2612.00	1825.00	5142.00	1147.00	280.00	1895.00	103.00
Mo	0.26	0.07	1.69	0.14	0.10	0.11	57.30	5.76	1.23
As	29224.00	329.00	3814.00	69.200	30.00	5339.00	4478.00	4324.00	110.00
Ag	0.01	0.03	0.01	0.01	0.02	<0.002	0.01	<0.002	0.01
Cd	0.02	0.05	<0.002	0.00	0.02	0.03	0.10	0.03	0.01
Sn	0.15	0.13	0.09	0.09	0.08	0.16	0.07	0.11	0.61
Sb	31.00	262.00	296.00	16.00	0.19	26.10	4.37	58.90	2.37
Ba	294.00	101.00	137.00	187.00	112.00	4307.00	6.39	90.00	12.90
Tl	0.50	0.71	1.16	0.07	0.01	1.01	0.23	2.16	0.01
Pb	0.12	0.36	0.39	0.14	0.06	0.05	0.10	0.04	0.73
Th	0.08	0.12	0.10	<0.002	0.02	0.05	0.07	0.03	0.03
U	0.04	0.04	0.03	0.04	0.13	0.02	0.01	0.02	1.93
$^{87}Sr/^{86}Sr$ (‰)	0.711531	0.742322	0.724661	0.714484	0.715482	0.711505	0.708902	0.712194	0.710253

medium-to high-temperature spring waters of the KKF are the another end-member of thermal water.

In addition, we plot the quartz solubility curve under the conditions of steam separation occurring (maximum steam loss) or not (no steam loss). In addition, the silica–enthalpy diagram can quantify the mixing ratio of cold water when thermal springs ascend. Based on a sequence of enthalpies and quartz solubilities in various temperatures, the fraction of cold water (X_t) can be calculated by the follow formula (Fournier and Truesdell, 1974):

$$X_t = \frac{(H_R - H_S)}{(H_R - H_C)}$$

where H_S is the enthalpy of hydrothermal spring water, H_C is the enthalpy of cold water, and H_R is the enthalpy of reservoir waters.

3.4 Circulation depth

The circulation depth of the geothermal fluids can be calculated as the following formula (Lu et al., 2017):

$$D = \frac{T - T_0}{G} + Z_0$$

where D is the circulation depth (km), T is the estimated reservoir temperature (°C), T_0 is the local annual average temperature (°C), G is the geothermal gradient (°C/km), and Z_0 is the thickness of the constant-temperature zone (km). For the samples of spring water collected along the Karakorum fault, the circulation depth was estimated by applying a local annual average temperature of 0.4°C (Wu et al., 2011), a constant-temperature zone at 30 m, and a regional geothermal gradient of 30°C/km (Chen et al., 2013).

4 Results

4.1 Physicochemical properties of the geothermal system

The geochemical compositions of the spring water samples collected along the KKF are presented in Table 1. Except for sample KK-9, a cold spring with a temperature of

6°C, all the spring water samples were from thermal springs with temperatures in the range of 48.5–83.4°C at the spring vent. The pH values of the spring water samples were 6.72–8.28 (neutral to alkaline), and the electrical conductivity (EC) and total dissolved solids (TDS) values varied widely, from 144.7 to 62,900 μS/cm and from 20.66 to 3,196.92 mg/L, respectively.

Based on the concentrations (Table 1) in milligram equivalents from high to low, the main cations of most of the spring water samples (excluding samples ZDGB-4, MS-5 and KK-9) were Na^+ (250.92–1,082.17 mg/L), K^+ (8.84–135.49 mg/L), Ca^{2+} (4.05–59.11 mg/L) and Mg^{2+} (0.21–21.65 mg/L). The major cationic concentrations in the sample collected from sample MS-5 were Mg^{2+} (177.65 mg/L) and Na^+ (225.44 mg/L). The major cationic concentrations in the samples collected from samples ZDGB-4 and KK-9 were Ca^{2+} (148.783 and 18 mg/L, respectively) and Na^+ (118.091 and 11.33 mg/L, respectively). The main anion in samples BEHZ-6, NM-7 and LJ-8 was Cl^- (179.87–1822.34 mg/L), while that in the rest of the samples was HCO_3^- (79.52–1,360.56 mg/L). The dissolved SiO_2 contents were 32.96–214.00 mg/L in the thermal springs and as low as 8.65 mg/L in the cold spring.

Trace elements were present in a wide range of concentrations (see Table 2), ranging from fractions to hundreds of thousands of μg/L. Boron (B), arsenic (As), lithium (Li), strontium (Sr), barium (Ba), iron (Fe) and antimony (Sb) were the most abundant elements, present at concentrations from 326.00 to 497,014.00 μg/L, 30.00–29,224.00 μg/L, 12.8–35,553.00 μg/L, 103.00–5,142.00 μg/L, 6.39–4,307.00 μg/L, 12.80–568.00 μg/L, and 0.19 μg/L to 293.00 μg/L, respectively. The Li, B, Sr and As concentrations were higher in the higher-temperature thermal springs than in the lower-temperature springs (samples ZDGB-4, MS-5 and KK-9) along the KKF, while the Fe, Cu, Zn, Sn, Pb and U concentrations in the thermal springs were lower than in the low-temperature springs. Compared to the concentrations of B, F, As and Li in typical high-temperature geothermal systems, such as the Kangding (Tang et al., 2017), Yangbajing (Guo et al., 2008, 2010), Yangyi (The Geothermal Geological Team of Tibet, 1990; Guo et al., 2009; Yuan et al., 2014), Rehai (Shangguan and Huo, 2002; Guo et al., 2014a, b) and Cuopu (J. Tian et al., 2019) systems in the Himalayan geothermal belt, those of the medium- to high-temperature geothermal springs along the KKF ranged from 3 to 497.01 mg/L, 1.44–15.08 mg/L, 0.03–29.22 mg/L, and 0.32–35.55 mg/L, respectively, which were consistent with the typical 'geothermal suite' (Kaasalainen et al., 2015).

4.2 Isotopic characteristics of the geothermal system

The stable oxygen and hydrogen isotopic compositions of the spring water samples from the KKF ranged from -16.8 to -13.3‰ and from -142.7 to -115.8‰, respectively, *versus* V-SMOW. The results are shown in Table 1. A plot of δD-$\delta^{18}O$ is shown in Table 1.

The Sr isotopic compositions of the spring water samples from the KKF region are shown in Table 2. The ratios varied from 0.7089 to 0.7423. Extremely radiogenic ratios (> 0.724) were detected for samples QP-2 and XB-3, which are adjacent to Lake Manasarovar.

5 Discussion

5.1 Origin of thermal springs

5.1.1 Hydrochemical features

Physicochemical parameters (such as temperature, EC and TDS) can be used to determine the water chemistry and circulation characteristics of groundwater. Our results demonstrate that geothermal spring water samples with higher temperatures exhibit higher EC (>1,000 μs/cm) and TDS (>650 mg/L) values than type A water (Table 1). In general, high EC values can be caused by high concentrations of dissolved minerals in water (Zainal et al., 2016). Higher TDS values reflect a longer circulation path and residence time (Belhai et al., 2016). Assuming that the springs belong to the same water source, geological context and thermal source, temperatures at the spring vent indicate the circulation depth, time of circulation and regional geothermal gradients (Zainal et al., 2016).

5.1.1.1 Major elements

The hydrochemical characteristics of most of the geothermal water samples analysed in this study were those of bicarbonate types besides samples BEHZ-6, NM-7 and LJ-8. The concentrations of major cations and anions of springs in the KKF (Table 2) are shown on a Piper diagram (Piper, 1944) (Figure 2) with three types of faces: (A) HCO_3–Mg·Na (sample MS-5) or HCO_3–Ca·Na (samples ZDGB-4 and KK-9); (B) HCO_3–Na (sample QP-2) or HCO_3·Cl–Na (samples DGQ-1 and XB-3); and (C) Cl–Na (sample BEHZ-6) or Cl·SO_4–Na (samples NM-7 and LJ-8). Type A water, especially the cold spring water (sample KK-9), is characteristic of shallow or subsurface water in the unsaturated zone and has high concentrations of Ca^{2+}, Mg^{2+} and HCO_3^-, which may be caused by the dissolution of Ca^{2+} and Mg^{2+} ions in a rock field of limestone and Marl+$CaSO_4$ origin (Appelo and Postma, 2004) or in the soil by meteoric water action (Hiscock, 2005). Therefore, considering the temperature measured at the spring vent, sample KK-9 (as a cold spring, 6°C), with type A water, can be classified as shallow and as having closed stable oxygen isotope characteristics with the local meteoric water (e.g., Shiquanhe station, $\delta^{18}O$: -14.4‰; altitude: 4,278 m) (Yao et al., 2013). Whereas the relatively high temperatures of samples ZDGB-4 and MS-5 (69.6°C and 48.5°C, respectively) may be influenced by mixing with thermal

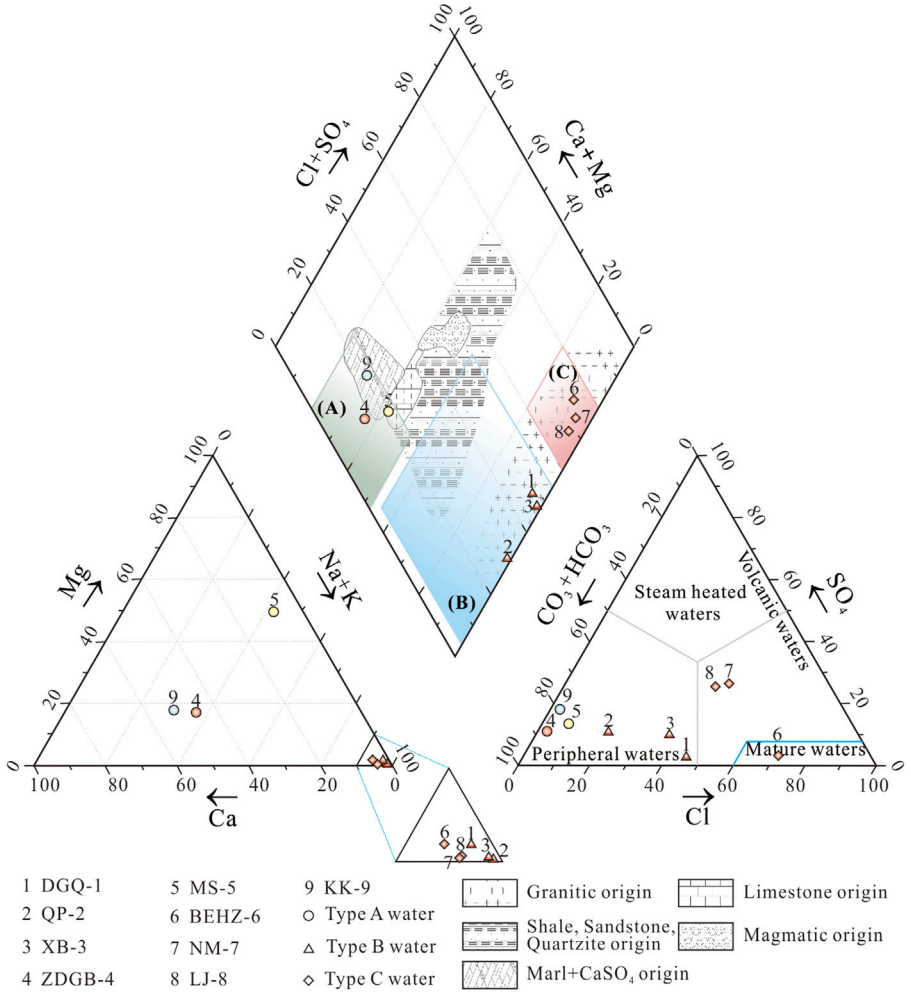

FIGURE 2
Piper diagram to recognise the hydrogeochemical facies in spring water samples from the KKF. Cl–SO_4–HCO_3 triangular diagram in the lower right corner of Piper diagram (based on Nicholson, 1993). The rock field in the Piper diagram was adopted from Zuurdeeg and Van der Weiden (1985) and Appelo and Postma (2004). The legend filled blue, yellow, and red color represent the temperatures at the spring vent below 25°C, between 25°C and 50°C, and above 50°C of spring water samples, respectively.

water. The A and B water types are bicarbonate-type spring waters formed by chemical reactions between infiltrated meteoric water and dissolved carbon dioxide, the distinction being that type B water may be formed by a reservoir rock field of granitic origin, according to the Piper diagram, that contains albite and microcline as the major minerals (J. Tian et al., 2019). In comparison to type A water, type B water is richer in Na^+ and deficient in Ca^{2+} and Mg^{2+} as a result of deep infiltration and water–rock interaction processes. The flow pattern of this type of water is characteristic of the evolution of groundwater (Stuyfzand, 1999). Unlike the two types mentioned above, type C water may represent thermal water that probably are at most the groundwater flow system with a long flow distance and long residence time in the aquifer. The Cl–Na-type spring shows that dissolution of chlorides prevails in sample BEHZ-6. In addition, samples NM-7 and LJ-8 are of the Cl·SO_4–Na type, indicating that the dissolution of chlorides and sulphates prevails in sample LJ-8.

Three groups of geothermal waters are shown in the lower right corner of Figure 2: steam-heated waters, mature waters and peripheral waters. Type A water and type B water are bicarbonate types. Both were plotted in the peripheral zone and are considered to be peripheral water with a relatively shallow heating hydrological circuit in the crust and no obvious material contribution from a magmatic fluid. Type C water samples are plotted in the chloride field. Among the type C water samples, sample BEHZ-6 plot in the chloride mature field is similar to typical high-temperature geothermal waters from

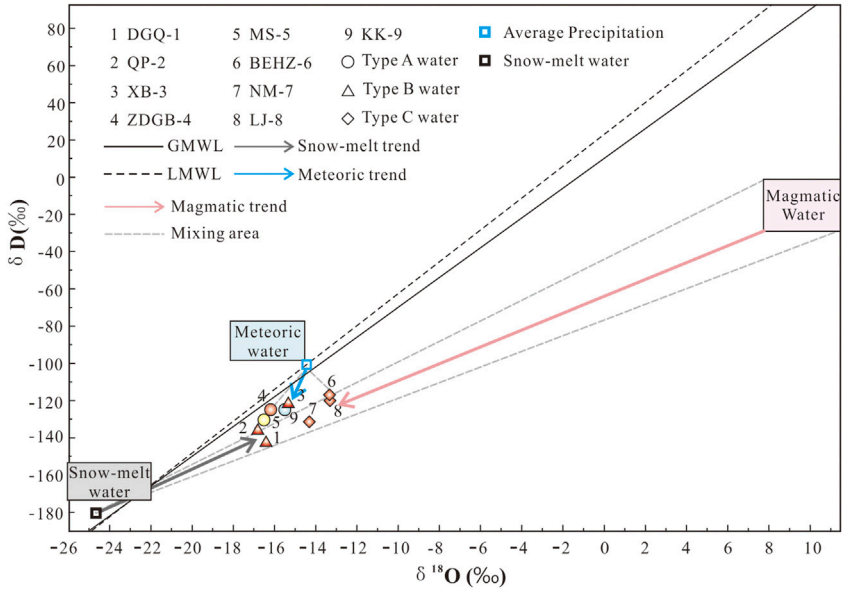

FIGURE 3
Plot of stable oxygen and hydrogen isotopes of spring water samples from the KKF. The straight line ($\delta D = 8.0\delta^{18}O + 10.0$; Craig, 1961) represents the global meteoric water line (GMWL), and the dashed line ($\delta D = 7.93\delta^{18}O + 11.59$) represents the local meteoric water line (LMWL) at the Gangotri station, India. V-SMOW = Vienna Standard Mean Ocean Water. The legend is the same as in Figure 2.

Yangbajing and the Yellowstone National Park, which are generally considered to be heated by underlying magma, and the water is affected by magmatic fluid (water and volatile) to various degrees. This conclusion is confirmed by the results of the analysis of oxygen and hydrogen isotopes (Figure 3), presented in section 5.1.2. It is widely recognized in the geothermal community that Cl^- in high concentrations in high–temperature geothermal fluids originates mainly from mixing with magmatic water (Guo et al., 2014a, b; Tian et al., 2018). Samples NM-7 and LJ-8 have lower HCO_3/Cl ratios than sample BEHZ-6 and fall in the chloride field away from the chloride mature field, suggesting these thermal water samples underwent fast-ascending partial mixing with near-surface water.

5.1.1.2 Trace elements

The enrichment factors (EF_i) of trace elements in spring waters along the Karakorum fault are shown in Figure 4. According to the concentrations of trace elements, the hot spring water is similar to granodiorite from the Jiangba pluton in the Shiquanhe area, with high concentrations of Li, Al, Fe, Sr, Ba and Pb, compared to other elements (Be, Ti, Cr, Co, Ni, Cu, Sn, Tl, and U), indicating that these elements in the hot spring water mainly originate from water–rock interactions. For instance, thermal water has high concentrations of Sr and Ba, 103–5,142 μg/L and 6.39–4,307 μg/L, respectively. It is assumed that the geothermal water in the study area has water–rock interaction with volcanic and magmatic rocks at the depth of the KKF. During this process, Sr and Ba in potassium feldspar and hornblende minerals in volcanic and magmatic rocks are often replaced with Ca and K in geothermal water, thus contributing Sr and Ba elements to the spring water. In addition, Sr is more easily migrated and occurs at a higher concentration than Ba in bicarbonate-type spring water. However, differences in the chemical properties and migration capacities of various trace elements lead to Be, Ni, Cu, Tl and U enrichment in addition to that of Li Sr, and Ba in some springs, compared to the granodiorite from the Jiangba pluton in the Shiquanhe area (Figure 4). Li is more enriched than other elements in the spring water samples, except for sample DGQ-1 (C_{Li} = 0.0128 mg/L), where its concentration was up to 16.935 mg/L. The enrichment factors for Al, V, Co, Pb, Sn and Th were less than 1, indicating sources of geothermal water other than the interaction of Jiangba pluton.

Previous studies on high-temperature geothermal systems have recognized Li, B, Fe and As being a typical 'geothermal suite' (Kaasalainen et al., 2015). The Li, B, Fe and As concentrations of type A water are 1–3 orders lower than those of type B and type C waters along the KKF (Table 2; Figure 5) and other typical high-temperature geothermal systems in the Tibetan Plateau (Guo et al., 2008, 2009, 2014a, b). This phenomenon is probably due to a shallow circulation depth of type A water, where there is no mantle-derived magmatic intrusion in the shallow crust supplying both heat and volatiles (J. Tian et al., 2019). The type B and C thermal waters along the KKF have high Li concentrations (> 0.96 mg/L), a signature of deep fluid upwelling. Hydrolysis of lithium silicate minerals (such as

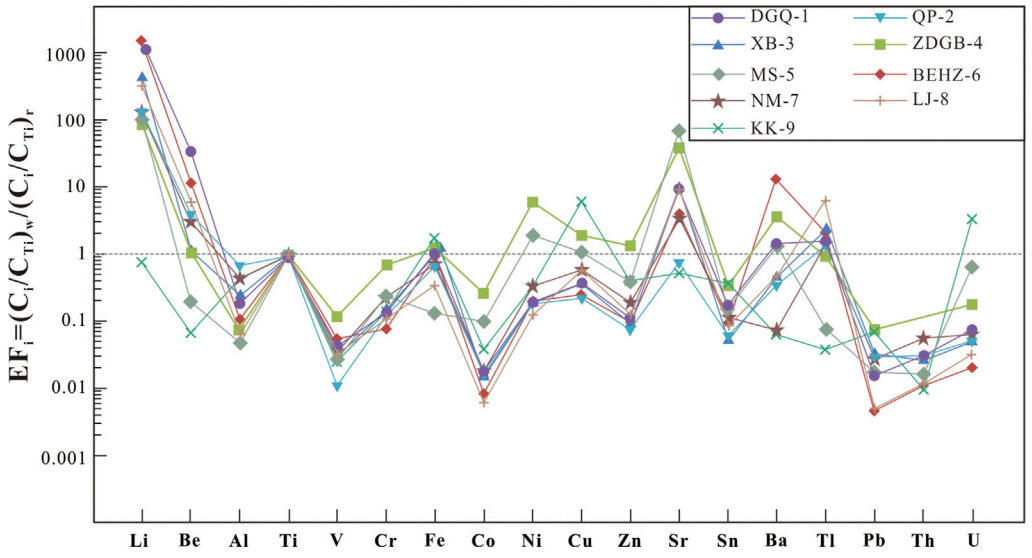

FIGURE 4
Trace element distribution for geothermal water samples along the KKF.

lepidolite and hydroxyapatite) in granites and granodiorite during deep circulation processes are speculated to result in the dissolution of Li entering thermal water (Zhang et al., 2003). As the solubility of boron (B) in geothermal water increases with depth, pressure and temperature (Zhang et al., 2003), a higher boron content in a water sample indicates a greater depth at which geothermal water is circulating. The relatively high boron contents of the type B and type C waters, shown in Figure 5, suggest deep circulation.

Arsenic (As), a toxic trace element, plays an important role in the study of geothermal resources. The arsenic concentrations of sample KK-9 vary widely (Figure 5; Table 2). The type B and type C waters have higher arsenic contents (0.33–29.22 mg/L) than the type A waters (0.03–0.11 mg/L), especially sample DGQ-1 having an extremely high arsenic concentration (as high as 29.22 mg/L), compared to those in typical high-temperature geothermal systems that are recognized as being influenced by underlying magma or hot thickened crust to different degrees (Guo et al., 2008, 2009, 2014a, b; Wang, 2021). The high arsenic concentrations in type B and type C waters may be related to Gangdese granitoids, deeper circulation and water–rock interaction. This is because arsenic in geothermal fluids mainly derives from the dissolution of arsenic from As-rich minerals in upper crustal rocks during water–rock interaction when deep circulation of geofluids occurs. Arsenic then migrates to the surface as geothermal fluids rise (Wang, 2021).

5.1.2 Hydrogen and oxygen stable isotopes

As shown in Figure 3, all the spring water samples fall near the global meteoric water line (GMWL) and the local meteoric water line (LMWL), providing significant information about the origin of geothermal water (Craig, 1961; Pang et al., 2017; Duan et al., 2022), i.e. that the springs are mainly recharged by infiltrated precipitation.

In this study, the local precipitation isotope data were selected for the Shiquanhe station ($\delta^{18}O$: -14.4‰; altitude: 4,278 m) of the Tibetan Network for Isotopes in Precipitation (TNIP) (Yao et al., 2013), which is the closest to the sampling sites. The $\delta^{18}O$ vertical gradient in the Tibetan Plateau was assumed to be -3.1‰/km (Yu et al., 1984). Consequently, the recharge elevation range (calculated as 4,568–5,052 m) for the KKF spring water samples was slightly higher than the elevation of the local meteoric water sampling point (4,278 m), excluding type C water (samples BEHZ-6, NM-7 and LJ-8). The recharge elevation is lower than the snow-capped mountain elevation around the locations of the spring water samples from the KKF area (5,500–6,000 m for the Gangdise mountains, 6,000 m for the Himalayan mountains, 5,500–6,000 m for the Kunlun mountains and 5,500–6,000 m for the Nyenchen Tanglha and Tanglha mountains). This suggests that the recharge source of all type A and B waters (excluding type C waters) is presumably not only meteoric water but also snowmelt water. Nevertheless, the recharge elevation of type C water was calculated to be 3,923–4,245 m, and type C water was more enriched in $\delta^{18}O$ (> -14‰) than type A and type B waters, which means that there should be other recharge sources. We speculate that magmatic waters enriched in D and ^{18}O may contribute to these geothermal fluids.

The $\delta^{18}O$ and δD values were plotted for the thermal springs and cold springs, as well as three end members

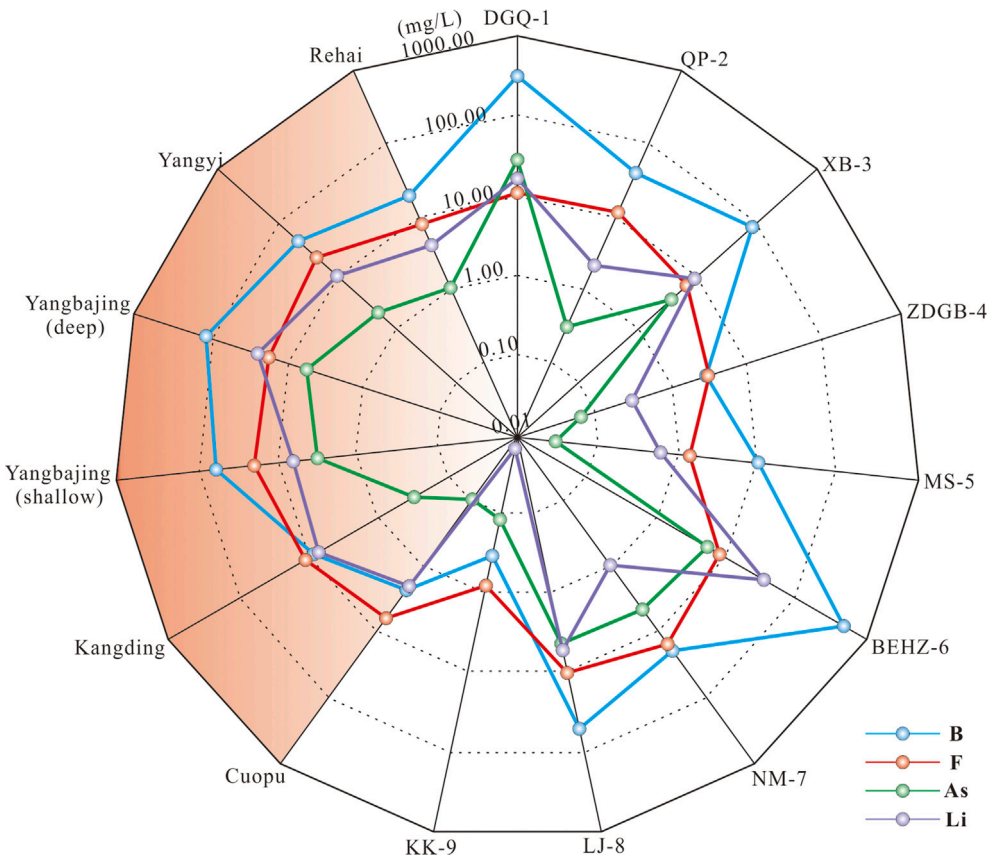

FIGURE 5
Concentrations of Li, B, F and As in geothermal waters along the KKF compared with those from typical high-temperature geothermal systems in the Himalayan geothermal belt (Guo et al., 2008, 2009; 2014; Wang, 2021).

(meteoric water, snowmelt water and magmatic water) (Figure 3). The snowmelt isotopes are referenced from glacier data (the Tanglang La in India, elevation 5,210 m) reported by Pande et al. (2000). The precipitation isotopes and the local meteoric water line are referenced from the Gangotri station, India, in GNIP (http://www-naweb.iaea.org/napc/ih/IHS_resources_gnip.html). The snowmelt water with δD of -180‰ and $\delta^{18}O$ of -24.7‰ falls to the lower left of the global meteoric water line (GMWL) and the local meteoric water line (LMWL), which can be explained by an isotopic fraction during the snow melting process and isotope altitude effect (Clark and Frintz, 1997). The weighted mean precipitation isotopes of the Gangotri station ($\delta^{18}O$: -14.5‰; δD: -103.7‰) plot on the LMWL or close to the GMWL. The magma water is enriched in δD and $\delta^{18}O$ within ranges of -20 ± 10‰ and 10 ± 2‰, respectively (Giggenbach, 1992).

Almost all the spring water samples fall into the mixing area among the three end members (Figure 3). At the mixing area, the type C water samples exhibit strong $\delta^{18}O$ enrichment and plot in the mixing zone between snowmelt water and magmatic water, suggesting that it is a mixture of snowmelt water and magmatic water. The mixing ratio of magmatic water in the spring waters was estimated to be 13%–17%. Type A and B waters in KKF are more likely to be influenced by evaporation or other factors than only by the magma water, so the actual mixing ratios are influenced by evaporation and other factors below 6%–13%.

An obvious oxygen isotope shift in geothermal waters is usually observed as a result of strong water–rock interaction when the rock is richer in $\delta^{18}O$ (Giggenbach, 1992). The positive $\delta^{18}O$ shift is generally ascribed to water–rock interactions affected by three factors: 1) the high temperature of reservoirs; 2) a long circulation time; 3) high ratios of rock to water (Tian et al., 2018). Nevertheless, no remarkable oxygen isotope shift ($\delta^{18}O$: -21.51‰ to -15.25‰; δD: -166.8‰ to -127.4‰) in the geothermal waters along the KKF was observed, which is consistent with numerous high-temperature geothermal systems in the Tibetan Plateau (Guo et al., 2010; Tan et al., 2014). This is probably because that the geothermal water circulates too quickly and stays too short a time within the reservoir to allow the water to attain full equilibrium between

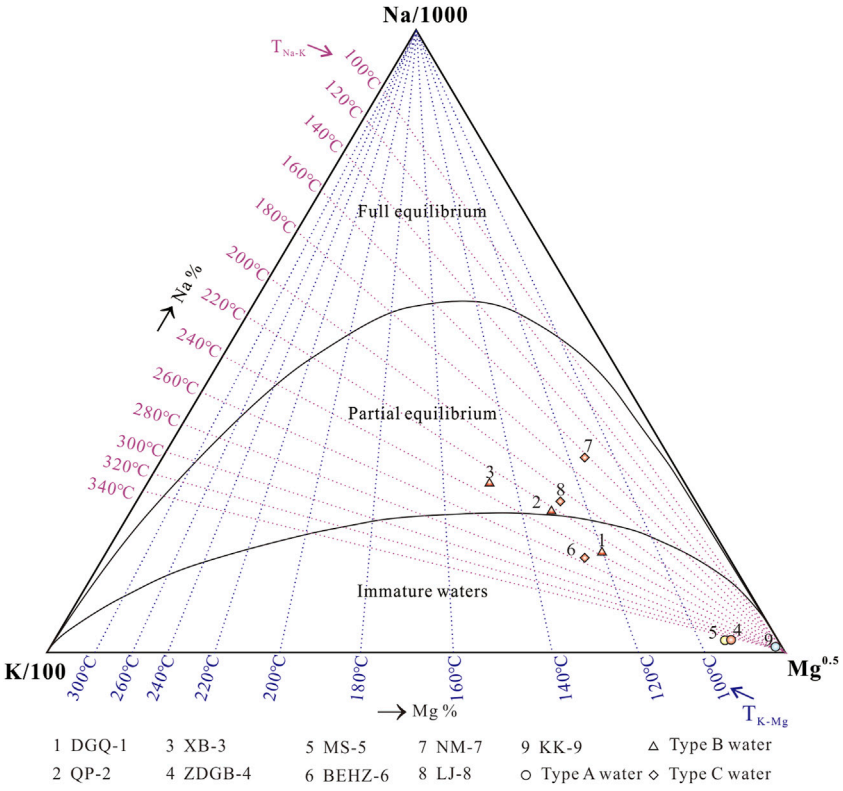

FIGURE 6
Giggenbach Na–K–Mg ternary diagram of spring water samples from the KKF. The legend is the same as in Figure 2.

water and rocks. This explanation is supported by the finding that none of the waters in the KKF region attain full equilibrium between water and rocks. As shown in Figure 3, the higher-temperature springs in the KKF area are slightly deficient in δD, with values ranging from -142.7 to -136.3‰ (type B water except for sample XB-3) or are more enriched in $\delta^{18}O$, with values ranging from -14.3 to -13.3‰ (type C water) than the lower-temperature springs (type A spring water). Therefore, the isotopic compositions with minimal oxygen isotopic shift of the type A water along the KKF could imply relatively shallower circulation or lower geothermal gradient than that of the type B and type C waters.

5.1.3 Water–rock interaction

Samples of DGQ-1, ZDGB-4, MS-5, BEHZ-6 and KK-9 is distributed in the immature water field (shallow or mixed waters), while samples QP-2, XB-3, NM-7 and LJ-8 is located in the partial equilibrium zone or mature field (Figure 6). The equilibrium temperatures of samples QP-2, XB-3, NM-7 and LJ-8 range from 160 to 240°C, indicating that these thermal waters came from deep and hot reservoirs. Therefore, they underwent water–rock interaction during the deep circulation process, and then were cooled with shallow cold water mixing during ascent. However, all the samples from the KKF are distributed in the immature water zone or partial equilibrium zone and away from the full equilibrium zone, indicating that none of these waters had attained full equilibrium between water and rocks. Type A water (samples ZDGB-4, MS-5 and KK-9) falls closer to the $Mg^{1/2}$ corner than the other water samples, indicating that mixed thermal waters are far from equilibrium and at low temperatures (Giggenbach, 1988). Therefore, the application of cation geothermometers such as Na–K and K–Mg thermometers to type A water would be problematic (Giggenbach, 1988). In contrast, types B and C waters are closer to the line of full equilibrium, indicating a slightly higher degree of water–rock interaction than type A water in the study area. This suggests a deeper or longer circulation which is less affected by the mixing process for type B and C waters. Thus, these springs can be used to estimate the reservoir temperature with cation geothermometers. An interesting point is that the type B waters (samples DGQ-1, QP-2 and XB-3) fall along the same isotherm of the reservoir temperature of ~ 220–240 °C (194.9–207.2 °C as calculated by the Na/K geothermometer), which suggests that they share a parent

TABLE 3 SI values of minerals in the spring waters along the Karakorum Fault.

Sample	DGQ-1	QP-2	XB-3	ZDGB-4	MS-5	BEHZ-6	NM-7	LJ-8	KK-9
Barite	−0.18	−0.30	0.06	−0.20	−0.11	1.21	−1.00	0.09	−0.86
Anhydrite	−2.51	−2.85	−2.28	−1.47	−2.03	−1.78	−2.01	−1.52	−3.05
Celestite	−1.94	−2.37	−1.18	−1.78	−1.23	−1.81	−1.96	−0.96	−3.34
Gypsum	−2.68	−3.11	−2.40	−1.58	−1.95	−1.95	−2.21	−1.76	−2.79
Alunite	−21.48	−21.42	−27.04	−2.27	−3.92	−15.22	−19.84	−22.84	0.86
Jarosite-K	−14.77	−17.44	−21.50	2.17	−6.32	−8.78	−15.30	−16.69	−4.43
Melanterite	−18.25	−19.84	−23.00	−8.16	−8.90	−14.39	−17.62	−19.14	−6.67
Calcite	1.11	0.73	1.26	1.30	0.20	1.10	0.54	1.22	−1.00
Aragonite	0.99	0.62	1.14	1.18	0.07	0.98	0.43	1.11	−1.16
Dolomite	2.36	1.11	1.86	2.49	1.46	2.21	−0.34	1.59	−2.64
Rhodochrosite	−0.47	−0.81	−0.96	2.29	−1.53	0.32	−0.32	0.24	−1.62
Siderite	−9.29	−10.80	−14.19	−0.13	−1.73	−6.17	−9.69	−10.97	−0.38
Strontianite	0.34	−0.08	0.98	−0.38	−0.49	−0.28	−0.73	0.48	−2.69
Witherite	−1.36	−1.39	−1.27	−2.30	−3.08	−0.71	−3.20	−1.87	−4.53
K-feldspar	−0.86	−0.22	−2.99	1.66	−0.11	1.16	−1.50	−1.43	0.82
Albite	−1.69	−0.93	−3.85	0.27	−1.83	0.24	−1.84	−2.08	−0.65
Anorthite	−3.08	−1.93	−4.48	2.47	−3.89	−1.46	−2.75	−3.60	−1.02
K-mica	0.23	1.54	−3.77	11.33	6.09	4.07	0.19	−1.69	12.38
Illite	−4.72	−4.36	−5.67	−0.44	−2.27	−3.81	−4.41	−5.37	0.15
Kaolinite	−3.70	−2.70	−7.68	4.57	0.49	−0.29	−3.99	−5.24	5.14
Ca-Montmorillonite	−3.62	−2.76	−7.27	5.37	2.17	−0.59	−2.92	−4.90	7.66
Sepiolite(d)	−5.49	−4.34	−10.57	4.69	0.63	−1.39	−4.67	−6.82	6.55
Sepiolite	1.23	0.55	1.82	−5.12	−6.63	0.02	−2.68	0.45	−8.29
Chrysotile	5.25	4.73	5.75	−1.20	−3.16	4.03	1.40	4.60	−5.92
Talc	11.07	10.32	13.89	0.71	−3.31	7.70	5.25	10.19	−9.54
Chlorite(14A)	14.93	14.50	15.88	4.88	0.75	12.75	9.26	14.22	−6.23
SiO_2(a)	18.46	18.06	21.46	9.56	−1.32	14.43	9.40	15.78	−8.17
Quartz	−0.88	−0.74	−1.81	−0.72	−0.72	−0.29	−0.81	−0.81	−0.96
Chalcedony	0.11	0.22	−0.80	0.30	0.40	0.71	0.17	0.15	0.44
Halite	−0.19	−0.06	−1.10	−0.01	0.04	0.41	−0.12	−0.13	−0.06
Fluorite	−5.02	−6.13	−4.96	−7.47	−6.53	−4.51	−6.06	−5.37	−9.29

geothermal fluid at depth but mix with cold water near the surface. This phenomenon further confirms that geothermal water rises along the same conduit underground until it is dispersed in the anisotropic porous Quaternary sediment (J. Tian et al., 2019).

5.1.4 Mineral saturation states (SI)

The mineral saturation index (SI) of geothermal springs reflects mineral thermodynamic behaviours and water–rock equilibrium processes (Wang et al., 2016). By the PHREEQC program, we calculated mineral saturation index values for the spring water samples collected along the KKF at the outflow temperature. The saturation index values obtained are shown in Table 3; Figure 7. Almost all the spring water samples were unsaturated (SI < 0) with respect to sulphates (anhydrite, celestite, gypsum, alunite, jarosite-K, melanterite), carbonates (siderite and witherite), feldspars (K-feldspar, albite, anorthite) and halite. Most carbonates (calcite, aragonite, dolomite, rhodochrosite, strontianite), barite, silica and fluorite were in equilibrium (SI ≈I) with spring water in the KKF at the outflow temperature. The calculated results for the slightly saturated calcite and aragonite at the outflow temperature were consistent with field observations of the calcareous sinter at the spring vent. All of the hot spring water samples were saturated (SI > 0) with respect to quartz except sample XB-3, possibly because of a mixture of cold or snowmelt water during the thermal water ascent, resulting in a reduction in the quartz solubility with decreasing temperature. Consequently, the temperature calculated using the quartz thermometer was lower than the true temperature.

Interestingly, SI with respect to some minerals vary greatly for the different spring water types. SI values with respect to

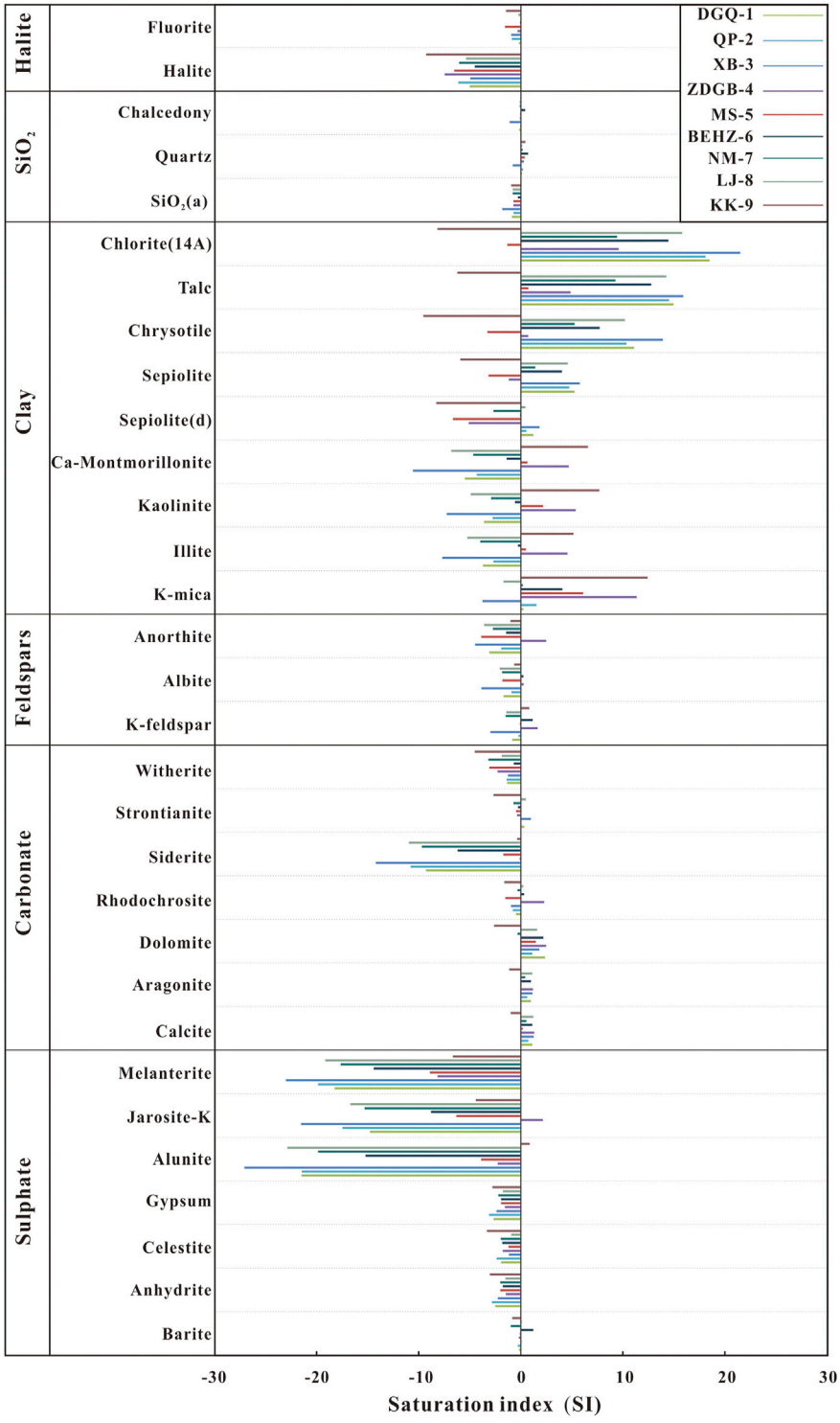

FIGURE 7
Saturation indexes of geothermal springs along the KKF zone at the outflow temperature.

siderite, Ca-montmorillonite, K-mica, illite and kaolinite (SI values from -1.73 to -0.13, -0.63 to 6.55, 6.09 to 12.38, 0.49 to 5.14 and 2.17 to 7.66, respectively) of Type A water is higher than that of type B and C waters (SI values from -14.19 to -6.17, -10.57 to -1.39, -3.77 to 4.07, -7.68 to -0.29 and -7.27 to -0.59, respectively). However, SI values with respect to

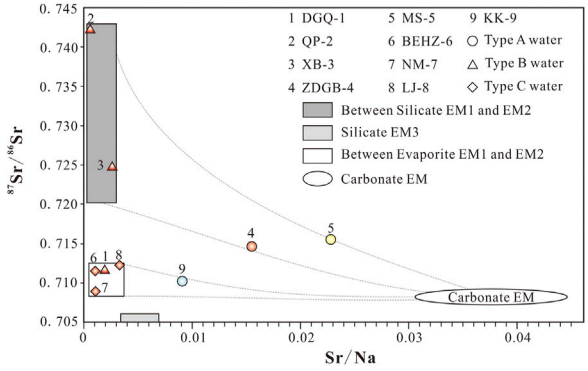

FIGURE 8
Plots of $^{87}Sr/^{86}Sr$ *versus* the corresponding Sr/Na for different spring waters from the KKF. The data for six end-members—silicate–EM1 (Gaillardet et al., 1999; Noh et al., 2009), silicate–EM2 (Xu and Liu, 2010), silicate–EM3 (Gaillardet et al., 1999; Noh et al., 2009), evaporite–EM1 (Liu et al., 2016), evaporite–EM2 (Moon et al., 2007; Xu and Liu, 2010), and carbonate–EM (Xu and Liu, 2010)—are based on lithological characteristics observed in China. The legend is the same as in Figure 2.

sepiolite, chrysotile, talc, and chlorite (SI values from -5.92 to -1.20, -9.54 to 0.71, -6.23 to 4.88 and -8.17 to 9.56, respectively) of type A water is lower than that of type B and type C waters (SI values from 1.40 to 5.75, 5.25–13.89, 9.26–15.88, 9.40–21.46, respectively). Relatively high SI values indicate high contents of these minerals and long residence times in the aquifer system. This phenomenon may reflect differences in the thermal reservoirs and the surrounding rock characteristics. For instance, oversaturation of typical hydrothermally altered minerals (sepiolite, chrysotile, talc and chlorite) in type B and type C waters indicates that Mg-rich carbonates are widely distributed due to hydrothermal alteration.

5.1.5 Strontium isotopic compositions

The results show a large range (0.708902–0.742322) for the $^{87}Sr/^{86}Sr$ ratios of the spring water samples from the KKF, which is consistent with the significantly variable $^{87}Sr/^{86}Sr$ ratios found in the terranes of the southern Tibetan Plateau (e.g., the Lhasa terrane, Qiangtang terrane and Himalaya Block) (Wang and Tang, 2020). The southern Tibetan Plateau, one of the most tectonically active regions, has an extremely complex geological setting, with a large amount of exposed Palaeozoic–Mesozoic sedimentary rock, low–high metamorphic rock and granitoids, contributing to the highly heterogeneous Sr isotope range. This suggests that differences in the Sr isotopic compositions of spring waters in the KKF region are largely dependent on the divergent geological conditions of the fracture zone.

The $^{87}Sr/^{86}Sr$ ratios against the corresponding Sr/Na values were plotted for different spring water samples (Figure 8) to examine the genesis of the Sr isotopic compositions. Samples QP-2 and XB-3, which are much more radiogenic (> 0.724) than the other springs (0.708–0.716), exhibit a mixing between silicate EM1 and silicate EM2, which is probably due to the influence of metamorphic rocks and granitoid sources (Gaillardet et al., 1999; Noh et al., 2009). Samples DGQ-1, BEHZ-6, NM-7 and LJ-8, which are less radiogenic (0.708–0.712) and exhibit low Sr/Na ratios (0.001–0.003), are distributed in the mixing range between evaporite EM1 and evaporite EM2, indicating that the evaporate dissolution plays an important role in these spring waters. The water samples from samples ZDGB-4, MS-5 and KK-9, with higher milligram equivalent percentages of Ca, Mg and HCO_3^- as well as Sr/Na ratios, are located closer to the carbonate EM than other samples, reflecting the strong influence of carbonate weathering on Sr isotopes. Samples ZDGB-4 and MS-5 are distributed along the mixing line of silicate and carbonate end-members, suggesting that the water from samples ZDGB-4 and MS-5 is more likely to be derived from silicate/carbonate weathering. The $^{87}Sr/^{86}Sr$–Sr/Na of sample KK-9 is located between the mixing lines of evaporite and carbonate end-members, which suggests that both of the carbonate rock weathering and evaporite dissolution contribute significantly to the $^{87}Sr/^{86}Sr$ ratios of sample KK-9.

5.2 Estimates of geothermal reservoir temperature

All the studied water samples from the KKF are ploted in the non-equilibrium field (partially equilibrated or immature) (Figure 9), indicating that none of these waters attained full equilibrium between water and rocks. Therefore, different multi-element geothermometers, such as Na–K and Na–K–Ca, may not reflect the true thermal reservoir temperature. In addition, meteoric water or snowmelt water mixing with ascending thermal water from the KKF leads to a

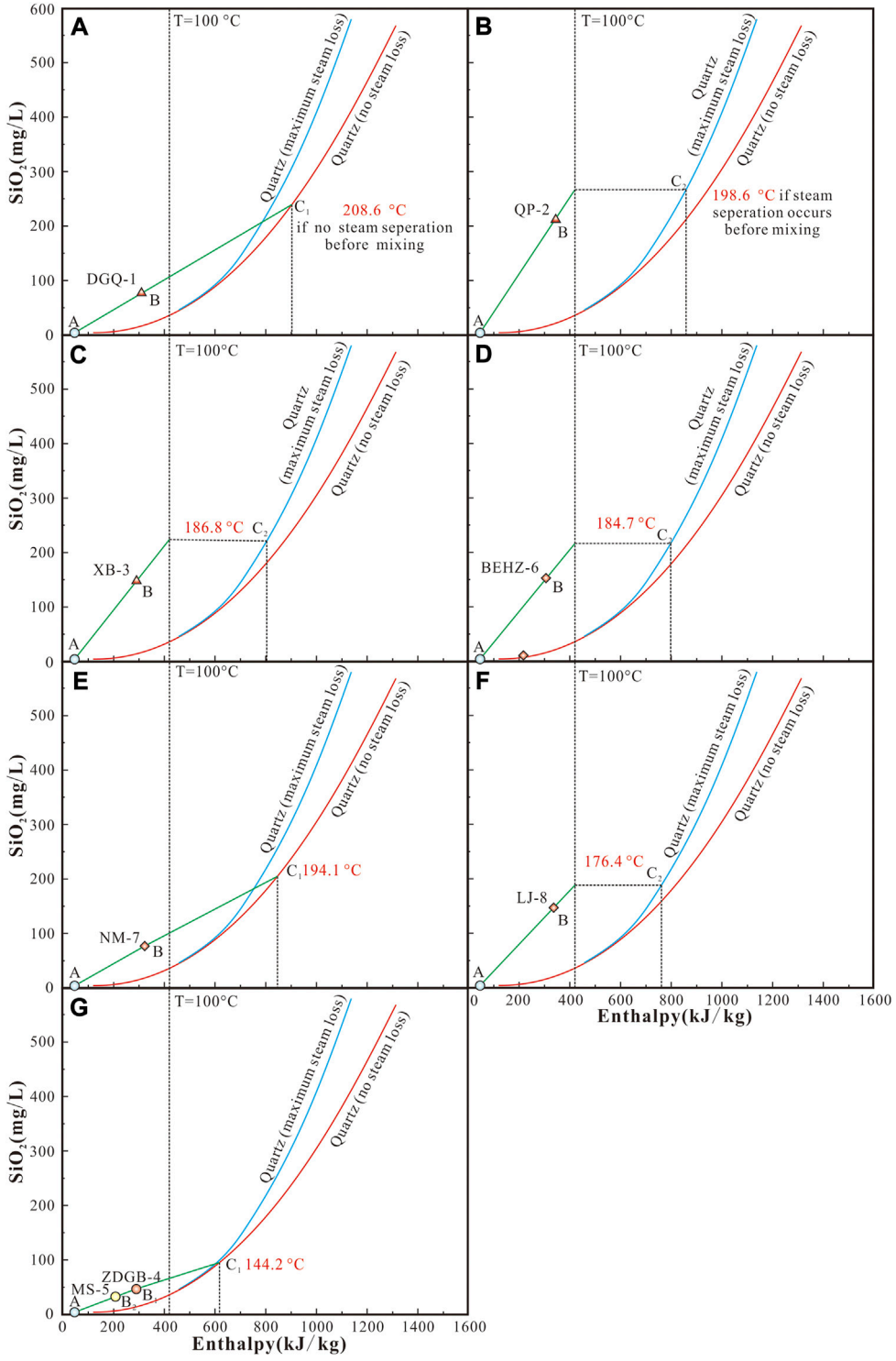

FIGURE 9
Plots of enthalpy *versus* silica for geothermal spring waters along the KKF. The legend is the same as in Figure 2.

decrease in SiO_2 concentration. Additionally, classical geothermometers (e.g., quartz geothermometers) mainly reflect the reservoir temperatures after the mixing of thermal water and cold water, the temperature calculated by quartz geothermometers is lower than the true thermal reservoir temperature before the mixing. The silica–enthalpy

TABLE 4 Calculated geothermometers of the geothermal fluids along the Karakorum Fault(°C).

Sample	Measured temperature	Silica geothermometers①				Cation geothermometers			Silica-enthalpy mixing model				Circulation depth (km)
		Quartz	Quartz (steam loss)	Chalcedony	Chalcedony (steam loss)	K/Mg②	Na/K③	Na-K-Ca④	Maximum steam loss		No steam loss		
									Enthalpy (kJ/kg)	Temperature	Enthalpy (kJ/kg)=	Temperature	
DGQ-1	75.0	125.8	123.1	97.9	98.5	121.0	207.2	235.6	–	–	903.6	208.6	7.0
QP-2	83.4	184.6	171.9	164.2	151.1	132.7	194.9	232.8	858.8	198.6	–	–	6.6
XB-3	70.0	161.0	152.6	137.2	130.0	148.9	202.6	276.2	806.1	186.8	–	–	6.2
ZDGB-4	69.6	98.8	99.97	68.67	74.18	83.3	341.1	102.0	–	–	616.9	144.2	4.8
MS-5	48.5	83.3	86.5	52.2	60.2	88.0	387.1	187.8	–	–	616.9	144.2	4.8
BEHZ-6	74.0	162.6	153.9	139.0	131.5	127.0	225.4	232.9	796.9	184.7	–	–	6.2
NM-7	77.9	123.3	120.9	95.1	96.2	114.3	139.6	121.1	–	–	839.0	194.1	6.5
LJ-8	81.2	160.1	151.8	136.2	129.2	129.4	183.9	186.0	759.9	176.4	–	–	5.9
KK-9	6.0	34.6	43.1	1.8	15.9	27.9	185.0	12.8	–	–	–	–	–

Note: Geothermometers are from ① Quartz geothermometer: If no loss of steam, $t(℃) = 1522/5.19 - \log SiO_2 - 273.15$; If maximum steam loss, $t(℃) = \frac{1522}{5.75-\log SiO_2} - 273.15$; Chalcedony geothermometer: If no loss of steam, $t(℃) = 1032/4.69 - \log SiO_2 - 273.15$; If maximum steam loss, $t(℃) = 1264/5.31 - \log SiO_2 - 273.15$ (Fournier, 1977); ② $T_{K/Mg} = 4410/13.95 - \log\ (K^2/Mg) - 273.15$ (Giggenbach, 1988); ③ $T_{Na/K} = 1052/1 + e^{(1.714\times\log(Na/K)+0.252)} + 76$ (Can, 2002); ④ $T_{Na-K-Ca} = 1647/\log(Na/K) + \beta(\log(\sqrt{Ca}/Na) + 2.06) + 2.47 - 273.15$ (Fournier, 1981).

10.3389/feart.2022.1021550

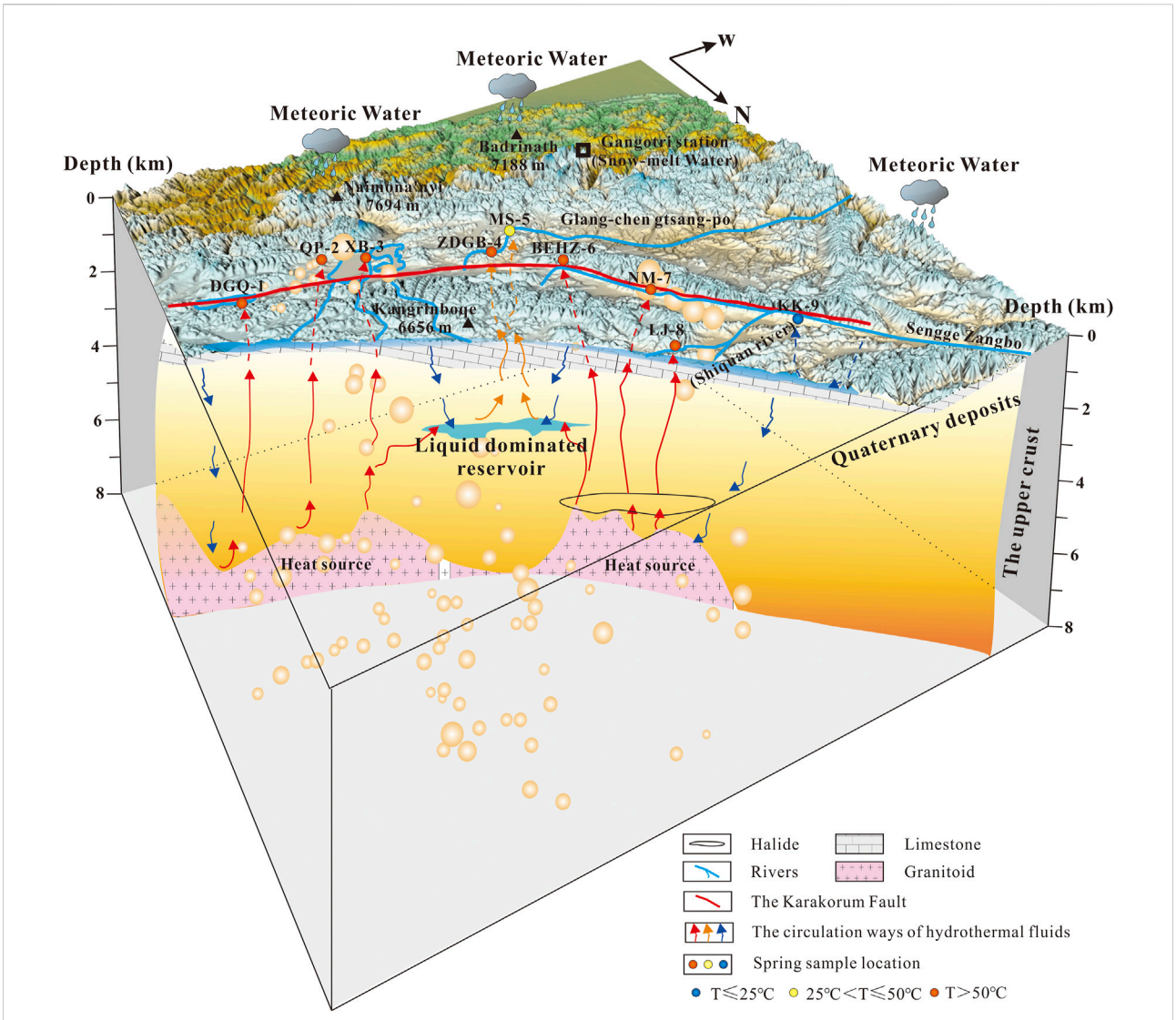

FIGURE 10
Conceptual hydrothermal model of the hydrogeochemical cycling process in high-temperature geothermal systems along the KKF. The red line and blue lines represent the main fault and rivers of the KKF, respectively. The blue, yellow, and red arrows represent the circulation pathways of hydrothermal fluids with low, intermediate, and high temperatures, respectively. The orange sphere shows the earthquakes that have occurred along the KKF within 200 km since 1970, and its dimensions (0.8–4.4 mm) correspond to the magnitude of the earthquake (M_L 1.0–5.9).

mixing model (Figure 9), as an available method for determining reservoir temperatures of spring water, was applied. For the samples of DGQ-1 (Figure 9A), NM-7 (Figure 9E), ZDGB-4 and MS-5 (Figure 9G), the extrapolations of the mixing lines from cold water (point A) to thermal water in the KKF have an intersection point C_1 with the quartz solubility curve (no steam loss). The intersection point C_1 suggests the enthalpy and SiO_2 concentration of the initial thermal fluid if there is no steam separation before mixing with cold water (largely meteoric water). It is noteworthy that samples ZDGB-4 and MS-5 are plotted on one mixing line (Figure 9G), suggesting that they have the same reservoir temperature. Nevertheless, for samples QP-2, XB-3, BEHZ-6 and LJ-8 with high SiO_2 concentrations (Figures 9B–D,F), no intersection point has been found between the extended mixing lines (from cold water to these thermal water) and the quartz solubility curve, indicating the presence of steam loss of thermal fluid before mixing with cold water during ascent. The mixing line from cold water to these thermal water has an intersection with a assumed vertical boiling line (100°C). Then, a horizontal line paralleling to the enthalpy axis was drawn from this intersection to intersect with the quartz solubility curve (maximum steam loss) at point C_2. The intersection point C_2 indicates the enthalpy and SiO_2 concentration when the thermal fluid begins to boil. In summary, the reservoir

temperatures of the deep geothermal reservoir were estimated by the silica–enthalpy mixing model, (Figure 9; Table 4), varying from 144.2°C to 208.6°C.

Moreover, the thermal water samples exhibit a wide range of mixing fractions with cold water quantified by the silica–enthalpy diagram, varying from 19% (sample QP-2) to 72% (sample MS-5). Varying mixing proportions of cold water indicate a remarkable decrease in temperatures (enthalpies) and dissolved silica concentrations. For instance, due to the different mixing proportions (57% and 72%, respectively) of cold water, different temperatures (69.6°C and 48.5°C, respectively) of spring vent were measured for samples ZDGB-4 and MS-5 in spite of the same reservoir temperatures (144.2°C) (Figure 9G).

5.3 Circulation model of geothermal fluid in the KKF

5.3.1 Estimates of geothermal circulation depth

Geothermal genesis can be categorised into three types: 1) magmatic genesis associated with active magma in the shallow crust; 2) radiogenic genesis related to the decay of radioactive elements in S-type granites; 3) tectonic deep circulation genesis related to regional tectonic movements, high background values of heat flow and deep circulation of geothermal water (Korhonen and Johnson, 2015; Wang, 2021). The KKF, a ~1,000-km-long strike–slip fault, has developed a series of extensional and transtensional fractures, which act as channels not only for groundwater infiltration but also for deep-derived geothermal fluid rising fluently. Many geothermal resources are widely distributed along the KKF. Previous geophysical studies of the geothermal system (He et al., 2016) described a low-resistivity anomaly characterized by resistivity in the range of 1–8 Ω m at a depth greater than 7 km, and suggested that the low-resistivity anomaly may be indicative of potentially partially melted magma in the upper crust, representing the heat source of the Qupu geothermal system. Furthermore, sample BEHZ-6 is located in the chloride mature field of the Cl–SO_4–HCO_3 diagram, similar to typical high-temperature geothermal waters from Yangbajing and Yellowstone National Park. According to previous studies, this high-temperature geothermal waters were heated by underlying magma since the Middle Palaeocene, and the water was affected by the magmatic fluid (water and volatile) to various degrees (Guo et al., 2014a, b; Tian et al., 2018). Nevertheless, there is insufficient evidence for volcanic activity in the KFF. Thus, we inferred that the high-temperature springs in the study area are primarily due to deep syntectonic hydrothermal circulation, and the dependence of the reservoir temperature on the heat source (the crustal rocks, e.g., granites) is largely controlled by the fault depth.

Based on the Na-K-$Mg^{1/2}$ diagram, the reasonable cation geothermometry and the silica–enthalpy mixing model, the reservoir temperature range of 144.6°C–208.6°C was determined for thermal water before mixing. The result for the circulation depth of geothermal fluids shows a wide range, from 4.8 km to 7.0 km (Table 4). As a result, the measured temperature at the spring vent is defined by the factor combining the mixing ratio of meteoric water or snowmelt water in the spring waters, the reservoir temperature and the circulation depth. Specifically, type A water with low temperature at the spring vent has a comparatively shallow circulation depth (4.8 km for samples ZDGB-4 and MS-5). In contrast, type B water (with circulation depths of 7.0 km, 6.6 km and 6.2 km for samples DGQ-1, QP-2 and XB-3, respectively) and type C water (with circulation depths of 6.2 km, 6.5 km and 5.9 km for samples BEHZ-6, NM-7 and LJ-8, respectively) have relatively large circulation depths.

5.3.2 Conceptual model

Combining the hydrochemistry characteristic, the recharge elevation, the reservoir temperature and the circulation depth of the spring water, we propose a conceptual model for the origin and evolution of geothermal fluid along the KKF (Figure 10). The geothermal water of the KKF is primarily recharged by local precipitation and melting ice water, which infiltrate to a depth of 4.8–7.0 km, and then are heated to 144.2–208.6°C during water–rock interaction with the Gangdese granitoids instead of underlying magmas. In the reservoir, the chemical reactions between water and the surrounding rocks (widely distributed granites and carbonate rockscontaining Na-rich minerals and carbonate minerals) result in the formation of geothermal water. The differences between type A water (HCO_3–Mg·Na or HCO_3–Ca·Na), type B water (HCO_3–Na) and type C water (Cl–Na or Cl·SO_4–Na) mainly depend on the type of surrounding rock, the circulation depth of the thermal fluid and the mixing ratio with cold water.

The circulation depth represents the lower limit of the fault depth. Therefore, the circulation depth estimated from the thermal reservoir temperature suggests a penetration depth of at least 7 km for the KKF. As shown in Figure 7, the location of medium-to high-temperature springs along the KKF is also an area of frequent occurrence of shallow earthquakes with minor magnitude. In addition, the epicentre depth was found to coincide with the circulation depth of the corresponding thermal water. This water participated in deep circulation and has been overpressured during water–rock interaction in an active fault system, which may drive the fluid flow and cause the fault weakening and seismicity. The important role of overpressured fluids palyedin the earthquake generation has been acknowledged by many researchers (e.g., Chiodini et al., 2011; Curzi et al., 2021). The frequent occurrence of earthquakes in turn weakens the crustal rocks and produces abundant fissures. These fissures are good for leaching out of the toxic

elements (e.g., As) from the surrounding rocks, and for migration of these elements to the surface by deep fluid ascent. The deeper the circulation happened, the more arsenic was leached from the crust during water–rock interaction, which can be evidenced by the arsenic concentrations in samples DGQ-1, QP-2, XB-3, BEHZ-6, NM-7 and LJ-8 are 1–3 orders of magnitude higher than that in samples ZDGB-4, MS-5 and KK-9 (Table 2; Figure 5). Overall, the geothermal water is significantly correlated with the epicentre and focal depth of earthquakes along the KKF, specifically in terms of the typical 'geothermal suite' (Li, B, F and As) and circulation depth of the thermal water.

In addition, the seismic catalogue shows that earthquakes along the KKF occur mostly at depths > 5 km, yet the traditional groundwater observation is dominated by shallow sources (< 5 km), so the traditional shallow groundwater are not involved in the inception process of deeper-source earthquakes but rather only as a passive post-earthquake response. Compared to shallow groundwater, geothermal fluids are less disturbed by the surface environment and human activities, which makes its utility in capturing realistic earthquake precursor information. Therefore, in addition to traditional groundwater observation stations, geothermal fluids is an effective supplement in forecasting earthquake, especially for short-term seismic prediction.

6 Conclusion

(1) Three types of the spring waters along the KKF were classified: type A water (HCO_3–Mg or HCO_3–Ca), type B water (HCO_3–Na) and type C water (Cl–Na or Cl·SO_4–Na). Type A and B waters are bicarbonate-type spring waters which were formed by chemical reactions among infiltrated meteoric water and dissolved carbon dioxide. Type A water was formed by the dissolution of Ca^{2+} and Mg^{2+} ions in rock fields of limestone and Marl+$CaSO_4$ origin, whereas type B water was formed by a reservoir rock field of granitic origin which contains albite and microcline as major minerals. Type C water was resulted from the dissolution of chlorides and sulphates.

(2) The Sr isotopic composition of type B water, except for sample DGQ-1, exhibits much more radiogenesis, which is resulted from the influence of metamorphic rocks and a granitoid source. Type C water and sample DGQ-1 are characterized by less radiogenesis and low Sr/Na ratios, indicating evaporate dissolution. The genesis of type A water is derived from the combined process of the dissolution of silicate/evaporite and infiltration of widespread carbonate rocks by meteoric water.

(3) Almost all of the spring waters were recharged mainly by infiltrated precipitation, with the recharge elevation range of 3.9–5.1 km. Type A and B waters were recharged not only by meteoric water but also by snowmelt water. Moreover, slightly anomalous ^{18}O enrichment occurs in type C water, indicating a water–rock interaction.

(4) Reservoir temperatures of 144.2–208.6°C and mixing ratios of 19%–72% were estimated. A conceptual model for geothermal fluid along the KKF was proposed, in which type A water with a low temperature at the spring vent has a comparatively shallow circulation depth, while type B and type C waters have relatively deep circulation depths (up to 7 km). The heat source of the geothermal system is resulted from the heating of crustal rocks rather than from the active magmas. The penetration depth of KKF is larger than 7 km.

(5) The geothermal water is significantly correlated with the epicentre and focal depth of earthquakes, especially for high-temperature spring water with deeper circulation and extremely high Li, B, Fe and As concentrations. Geothermal fluids can be used as a supplementary indicator in forecasting earthquake.

Data availability statement

The original contributions presented in the study are included in the article/Supplementary Material, further inquiries can be directed to the corresponding authors.

Author contributions

JW: data curation, validation, and writing—original draft. XZ: conceptualization, supervision, funding acquisition, and writing—review and editing. MH: investigation. JL: data curation. JD: formal analysis. JT: investigation. YY: data curation. YL: conceptualization. KL: data curation. YL: supervision, methodology, and writing—review and editing.

Funding

This research was financially supported by Central Public-interest Scientific Institution Basal Research Fund (CEAIEF2022030205, CEAIEF20220507, CEAIEF20220213), Special Fund of the Institute of Earthquake Forecasting (2021IEF0101, 2021IEF1201), Open Fund of Earthquake Forecasting, China Earthquake Administration (XH22034D), National Key Research and Development Project (2017YFC1500501-05, 2019YFC1509203), National Natural Science Foundation of China (41803035, 41802212, 41673106, 42073063, 4193000170), International Geoscience Program (724).

Acknowledgments

The authors are grateful to the editor and reviewers for constructive comments and suggestions. The authors benefitted a lot from the assistance of Yihai Yang, Yurong Qiu and Xinyan Li and Wei Tao.

Conflict of interest

The authors declare that the research was conducted in the absence of any commercial or financial relationships that could be construed as a potential conflict of interest.

The handling editor MZ declared a past co-authorship with the author XZ.

Publisher's note

All claims expressed in this article are solely those of the authors and do not necessarily represent those of their affiliated organizations, or those of the publisher, the editors and the reviewers. Any product that may be evaluated in this article, or claim that may be made by its manufacturer, is not guaranteed or endorsed by the publisher.

References

Appelo, C. A. J., and Postma, D. (2004). *Geochemistry, groundwater and pollution*. Florida, FL, USA: CRC Press. doi:10.1201/9781439833544

Banerjee, P., and Bürgmann, R. (2002). Convergence across the northwest Himalaya from GPS measurements. *Geophys. Res. Lett.* 29 (13), 16521–17304. doi:10.1029/2002gl015184

Barberio, M. D., Gori, F., Barbieri, M., Billi, A., Caracausi, A., De Luca, G., et al. (2020). New observations in Central Italy of groundwater responses to the worldwide seismicity. *Sci. Rep.* 10, 17850. doi:10.1038/s41598-020-74991-0

Belhai, M., Fujimitsu, Y., Bouchareb Haouchine, F. Z., Iwanaga, T., Noto, M., and Nishijima, J. (2016). Hydrogeochemical and isotope geochemical study of northwestern Algerian thermal waters. *Arab. J. Geosci.* 9 (3), 169–217. doi:10.1007/s12517-015-2252-2

Bianchi, A., Bovini, L., Botti, F., Doveri, M., Lelli, M., Manzella, A., et al. "Multidisciplinary approach to the study of the relationships between shallow and deep circulation of geofluids," in Proceedings of the World geothermal congress, Bali, Indonesia, April 2010, 25–29.

Brahim, F. B., Boughariou, E., Makni, J., and Bouri, S. (2020). Evaluation of groundwater hydrogeochemical characteristics and delineation of geothermal potentialities using multi criteria decision analysis: Case of Tozeur region, Tunisia. *Appl. Geochem.* 113, 104504.

Can, I. (2002). A new improved Na/K geothermometer by artificial neural networks. *Geothermics* 31 (6), 751–760. doi:10.1016/s0375-6505(02)00044-5

Chen, H. H., Wu, Y., and Xiao, Q. G. (2013). Thermal regime and Paleogeothermal gradient evolution of Mesozoic Cenozoic sedimentary basins in the Tibetan Plateau, China. *Earth Sci. J. China Univ. Geosciences* 38 (3), 541–552. doi:10.1016/S0264-3707(00)00002-8

Chen, Z., Zhou, X. C., Du, J. G., Xie, C. Y., Liu, L., Li, Y., et al. (2015). Hydrochemical characteristics of the hot spring waters in the Kangding district related to the Lushan MS 7.0 earthquake in Sichuan, China. *Nat. Hazards Earth Syst. Sci.* 2, 7293–7308. doi:10.5194/nhess-15-1149-2015

Chiodini, G., Caliro, S., Cardellini, C., Frondini, F., Inguaggiato, S., and Matteucci, F. (2011). Geochemical evidence for and characterization of CO_2 rich gas sources in the epicentral area of the Abruzzo 2009 earthquakes. *Earth Planet. Sci. Lett.* 304 (3–4), 389–398. doi:10.1016/j.epsl.2011.02.016

Clark, I. D., and Frintz, P. (1997). *Environmental isotopes in hydrogeology*. Boca Raton: Lewis & Co. doi:10.1201/9781482242911

Craig, H. (1961). Isotopic variations in meteoric waters. *Science* 133, 1702–1703. doi:10.1126/science.133.3465.1702

Curzi, M., Bernasconi, S. M., Billi, A., Boschi, C., Aldega, L., Franchini, S., et al. (2021). U–Pb age of the 2016 Amatrice earthquake causative fault (Mt. Gorzano, Italy) and paleo fluid circulation during seismic cycles inferred from inter and co-seismic calcite. *Tectonophysics* 819, 229076. doi:10.1016/j.tecto.2021.229076

Daniele, L., Taucare, M., Viguier, B., Arancibia, G., Aravena, D., Roquer, T., et al. (2020). Exploring the shallow geothermal resources in the Chilean southern volcanic zone: Insight from the liquine thermal springs. *J. Geochem. Explor.* 218, 106611. doi:10.1016/j.gexplo.2020.106611

Du, J. G., Liu, C. Q., Fu, B. H., Ninomiya, Y., Zhang, Y. L., Wang, C. Y., et al. (2005). Variations of geothermometry and chemical isotopic compositions of hot spring fluids in the Rehai geothermal field, southwestern China. *J. Volcanol. Geotherm. Res.* 142 (3–4), 243–261. doi:10.1016/j.jvolgeores.2004.11.009

Duan, R., Li, P. Y., Wang, L., He, X. D., and Zhang, L. (2022). Hydrochemical characteristics, hydrochemical processes and recharge sources of the geothermal systems in Lanzhou City, northwestern China. *Urban Clim.* 43, 101152. doi:10.1016/j.uclim.2022.101152

Faure, G. (1977). *Principles of isotope geology*. New York, NY, USA: John Wiley & Sons.

Fournier, R. O. (1981). "Application of water geochemistry to geothermal exploration and reservoir engineering," in *Geothermal systems: Principles and case histories*. Editors L. Rybach and L. J. P. Muffler (New York, NY, USA: John Wiley & Sons), 109–143.

Fournier, R. O. (1977). Chemical geothermometers and mixing models for geothermal systems. *Geothermics* 5 (1–4), 41–50. doi:10.1016/0375-6505(77)90007-4

Fournier, R. O., and Truesdell, A. H. (1974). Geochemical indicators of subsurface temperature—Part 2, estimation of temperature and fraction of hot water mixed with cold water. *J. Res. U. S. Geol. Surv.* 2, 263–270. doi:10.3133/ofr741032

Franchini, S., Agostini, S., Barberio, M. D., Barbieri, M., Billi, A., Boschetti, T., et al. (2021). HydroQuakes, central Apennines, Italy: Towards a hydrogeochemical monitoring network for seismic precursors and the hydro-seismo-sensitivity of boron. *J. Hydrology* 598, 125754. doi:10.1016/j.jhydrol.2020.125754

Frei, K. M., and Frei, R. (2011). The geographic distribution of strontium isotopes in Danish surface waters–a base for provenance studies in archaeology, hydrology and agriculture. *Appl. Geochem.* 26, 326–340. doi:10.1016/j.apgeochem.2010.12.006

Gaillardet, J., Dupré, B., Louvat, P., and Allègre, C. J. (1999). Global silicate weathering and CO_2 consumption rates deduced from the chemistry of large rivers. *Chem. Geol.* 159, 3–30. doi:10.1016/s0009-2541(99)00031-5

Giggenbach, W. F. (1988). Geothermal solute equilibria. derivation of Na–K–Mg–Ca geoindicators. *Geochimica Cosmochimica Acta* 52 (12), 2749–2765. doi:10.1016/0016-7037(88)90143-3

Giggenbach, W. F., Gonfiantini, R., Jangi, B. L., and Truesdell, A. H. (1983). Isotopic and chemical composition of parbati valley geothermal discharges, North-West Himalaya, India. *Geothermics* 12, 199–222. doi:10.1016/0375-6505(83)90030-5

Giggenbach, W. F. (1992). Isotopic shifts in waters from geothermal and volcanic systems along convergent plate boundaries and their origin. *Earth Planet. Sci. Lett.* 113 (4), 495–510. doi:10.1016/0012-821x(92)90127-h

Guo, Q. (2012). Hydrogeochemistry of high-temperature geothermal systems in China: A review. *Appl. Geochem.* 27 (10), 1887–1898. doi:10.1016/j.apgeochem.2012.07.006

Guo, Q., Liu, M., Li, J., Zhang, X., and Wang, Y. (2014a). Acid hot springs discharged from the Rehai hydrothermal system of the tengchong volcanic area (China): Formed via magmatic fluid absorption or geothermal steam heating? *Bull. Volcanol.* 76 (10), 868–912. doi:10.1007/s00445-014-0868-9

Guo, Q., Nordstrom, D. K., and McCleskey, R. B. (2014b). Towards understanding the puzzling lack of acid geothermal springs in Tibet (China): Insight from a comparison with Yellowstone (USA) and some active volcanic hydrothermal systems. *J. Volcanol. Geotherm. Res.* 288, 94–104. doi:10.1016/j.jvolgeores.2014.10.005

Guo, Q., and Wang, Y. (2012). Geochemistry of hot springs in the Tengchong hydrothermal areas, Southwestern China. *J. Volcanol. Geotherm. Res.* 215, 61–73. doi:10.1016/j.jvolgeores.2011.12.003

Guo, Q., Wang, Y., and Liu, W. (2008). B, As, and F contamination of river water due to wastewater discharge of the Yangbajing geothermal power plant, Tibet, China. *Environ. Geol.* 56 (1), 197–205. doi:10.1007/s00254-007-1155-2

Guo, Q., Wang, Y., and Liu, W. (2009). Hydrogeochemistry and environmental impact of geothermal waters from Yangyi of Tibet, China. *J. Volcanol. Geotherm. Res.* 180 (1), 9–20. doi:10.1016/j.jvolgeores.2008.11.034

Guo, Q., Wang, Y., and Liu, W. (2010). O, H, and Sr isotope evidences of mixing processes in two geothermal fluid reservoirs at Yangbajing, Tibet, China. *Environ. Earth Sci.* 59 (7), 1589–1597. doi:10.1007/s12665-009-0145-y

Hajj, F., Poszwa, A., Bouchez, J., and Guérold, F. (2017). Radiogenic and "stable" strontium isotopes in provenance studies: A review and first results on archaeological wood from shipwrecks. *J. Archaeol. Sci.* 86, 24–49. doi:10.1016/j.jas.2017.09.005

He, L. F., Chen, L., Xi, X. L., Zhao, X. F., Chen, R. J., Yao, H. C., et al. (2016). Mapping the geothermal system using AMT and MT in the mapamyum (QP) field, Lake Manasarovar, southwestern Tibet. *Energies* 9 (10), 855. doi:10.3390/en9100855

Hiscock, K. M. (2005). "Hydrogeology. Principles and practice," in *Chemical hydrogeology*. Editor M. A. Malden (New york, NY, USA: Wiley Blackwell). doi:10.1111/j.1468-8123.2005.00118.x

Hu, X. M., Garzanti, E., Moore, T., and Raffi, I. (2015). Direct stratigraphic dating of India Asia collision onset at the Selandian (middle Paleocene, 59 ± 1 Ma). *Geology* 43, 859–862. doi:10.1130/g36872.1

Kaasalainen, H., Stefánsson, A., Giroud, N., and Arnórsson, S. (2015). The geochemistry of trace elements in geothermal fluids, Iceland. *Appl. Geochem.* 62, 207–223. doi:10.1016/j.apgeochem.2015.02.003

Kapp, P., Murphy, M. A., Yin, A., Harrison, T. M., Ding, L., and Guo, J. (2003). Mesozoic and cenozoic tectonic evolution of the Shiquanhe area of Western Tibet. *Tectonics* 22 (4), 1029. doi:10.1029/2001tc001332

Klemperer, S. L., Kennedy, B. M., Sastry, S. R., Makovsky, Y., Harinarayana, T., and Leech, M. L. (2013). Mantle fluids in the karakoram fault: Helium isotope evidence. *Earth Planet. Sci. Lett.* 366, 59–70. doi:10.1016/j.epsl.2013.01.013

Knappett, P. S. K., Li, Y. M., Hernandez, H., Rodriguez, R., Aviles, M., Deng, C., et al. (2018). Changing recharge pathways within an intensively pumped aquifer with high fluoride concentrations in Central Mexico. *Sci. Total Environ.* 622–623, 1029–1045. doi:10.1016/j.scitotenv.2017.12.031

Korhonen, F. J., and Johnson, S. P. (2015). The role of radiogenic heat in prolonged intraplate reworking: The Capricorn Orogen explained? *Earth Planet. Sci. Lett.* 428, 22–32. doi:10.1016/j.epsl.2015.06.039

Kundu, B., Yadav, R. K., Bali, B. S., Chowdhury, S., and Gahalaut, V. K. (2014). Oblique convergence and slip partitioning in the NW Himalaya: Implications from GPS measurements. *Tectonics* 33, 2013–2024. doi:10.1002/2014tc003633

Lacassin, R., Valli, F., Arnaud, N., Leloup, P. H., Paquette, J. L., Haibing, L., et al. (2004). Large-scale geometry, offset and kinematic evolution of the Karakorum fault, Tibet. *Earth Planet. Sci. Lett.* 219 (3–4), 255–269. doi:10.1016/s0012-821x(04)00006-8

Liu, H. B., Jin, G. S., Li, J. J., Han, J., Zhang, J. F., Zhang, J., et al. (2013). Determination of stable isotope composition in uranium geological samples. *World Nucl. Geosci.* 30 (3), 174–179. doi:10.1016/j.clay.2020.105736

Liu, W. J., Jiang, H., Shi, C., Zhao, T., Liang, C. S., Hu, J., et al. (2016). Chemical and strontium isotopic characteristics of the rivers around the badain jaran desert, northwest China: Implication of river solute origin and chemical weathering. *Environ. Earth Sci.* 75, 1119. doi:10.1007/s12665-016-5910-0

Lu, G. P., Wang, X., Li, F. S., Xu, F., Wang, Y. X., Qi, S. H., et al. (2017). Deep geothermal processes acting on faults and solid tides in coastal Xinzhou geothermal field, Guangdong, China. *Phys. Earth Planet. Interiors* 264, 76–88. doi:10.1016/j.pepi.2016.12.004

Lu, R. K., Li, Y., Sun, S. L., Liu, Y. M., Nan, G. W., Cui, H. F., et al. (2022). Middle triassic remnant of the palaeo tethys ocean, central Tibet: Constraints from the pianshishan retrograded eclogite type rocks. *Geol. J.* 57 (8), 3033–3047. doi:10.1002/gj.4453

Molnar, P., and Tapponnier, P. (1975). Cenozoic Tectonics of Asia: Effects of a Continental Collision: Features of recent continental tectonics in Asia can be interpreted as results of the India-Eurasia collision. *Science* 189, 419–426. doi:10.1126/science.189.4201.419

Moon, S., Huh, Y., Qin, J., and van Pho, N. (2007). Chemical weathering in the hong (red) river basin: Rates of silicate weathering and their controlling factors. *Geochimica Cosmochimica Acta* 71, 1411–1430. doi:10.1016/j.gca.2006.12.004

Nábělek, J., Hetényi, G., Vergne, J., Sapkota, S., Kafle, B., Jiang, M., et al. (2009). The hi-climb teamUnderplating in the himalaya-tibet collision zone revealed by the hi-CLIMB experiment. *Science* 325, 1371–1374. doi:10.1126/science.1167719

Nelson, K. D., Zhao, W. J., Brown, L. D., Kuo, J., Che, J. K., Liu, X. W., et al. (1996). Partially molten middle crust beneath southern Tibet: Synthesis of project INDEPTH results. *Science* 274, 1684–1688. doi:10.1126/science.274.5293.1684

Nicholson, K. (1993). *Geothermal fluids: Chemistry and exploration techniques*. New York NY, USA: Springer Verlag Berlin Heidelberg.

Noh, H., Huh, Y., Qin, J., and Ellis, A. (2009). Chemical weathering in the three rivers region of eastern Tibet. *Geochimica Cosmochimica Acta* 73, 1857–1877. doi:10.1016/j.gca.2009.01.005

Pande, K., Padia, J. T., Ramesh, R., and Sharma, K. K. (2000). Stable isotope systematics of surface water bodies in the Himalayan and Trans Himalayan (Kashmir) region. *J. Earth Syst. Sci.* 109 (1), 109–115. doi:10.1007/bf02719154

Pang, Z. H., Kong, Y. L., Li, J., and Tian, J. (2017). An isotopic geoindicator in the hydrological cycle. *Procedia Earth Planet. Sci.* 17, 534–537. doi:10.1016/j.proeps.2016.12.135

Pang, Z. H. (2006). pH dependant isotope variations in arc type geothermal waters: New insights into their origins. *J. Geochem. Explor.* 89 (1–3), 306–308. doi:10.1016/j.gexplo.2005.12.006

Parkhurst, D. L., and Appelo, C. A. J. (1999). *User's guide to PHREEQC (version 2): A computer program for speciation, batch reaction, one dimensional transport and inverse geochemical calculations*. Washington, DC, USA: United States Geological Survey (USGS), Water Resources Investigations Report, 312. doi:10.3133/wri994259

Piper, A. M. (1944). A graphic procedure in the geochemical interpretation of water analyses. *Trans. AGU.* 25 (6), 914–928. doi:10.1029/tr025i006p00914

Priestley, K., Jackson, J., and McKenzie, D. (2008). Lithospheric structure and deep earthquakes beneath India, the Himalaya and southern Tibet. *Geophys. J. Int.* 172, 345–362. doi:10.1111/j.1365-246X.2007.03636.x

Rai, S. S., Priestley, K., Gaur, V. K., Mitra, S., Singh, M. P., and Searle, M. (2006). Configuration of the Indian moho beneath the NW Himalaya and ladakh. *Geophys. Res. Lett.* 33, L15308. doi:10.1029/2006GL026076

Sachan, H. K., Santosh, M., Prakash, D., Kharya, A., Singh, P. C., and Rai, S. K. (2016). Metamorphic P–T conditions and CO_2 influx history of medium grade metapelites from Karakorum, Trans Himalaya, India. *J. Asian Earth Sci.* 124, 126–138. doi:10.1016/j.jseaes.2016.04.019

Schwab, M., Ratschbacher, L., Siebel, W., McWilliams, M., Minaev, V., Lutkov, V., et al. (2004). Assembly of the Pamirs: Age and origin of magmatic belts from the southern Tien Shan to the southern Pamirs and their relation to Tibet. *Tectonics* 23, TC4002. doi:10.1029/2003TC001583

Shangguan, Z., and Huo, W. (2002). δD values of escaped H_2 from hot springs at the Tengchong Rehai geothermal area and its origin. *Chin. Sci. Bull.* 47, 146–149. doi:10.1360/02tb9034

Skelton, A., Liljedahl-Claesson, L., Wästeby, N., Andrén, M., Stockmann, G., Sturkell, E., et al. (2019). Hydrochemical changes before and after earthquakes based on long-term measurements of multiple parameters at two sites in northern Iceland-a review. *J. Geophys. Res. Solid Earth* 124, 2702–2720. doi:10.1029/2018jb016757

Stuyfzand, P. J. (1999). Patterns in groundwater chemistry resulting from groundwater flow. *Hydrogeology J.* 7 (1), 15–27. doi:10.1007/s100400050177

Tan, H., Zhang, Y., Zhang, W., Kong, N., Zhang, Q., and Huang, J. (2014). Understanding the circulation of geothermal waters in the Tibetan Plateau using oxygen and hydrogen stable isotopes. *Appl. Geochem.* 51, 23–32. doi:10.1016/j.apgeochem.2014.09.006

Tang, X. C., Zhang, J., Pang, Z. H., Hu, S. B., Wu, Y., and Bao, S. J. (2017). Distribution and Genesis of the eastern Tibetan Plateau geothermal belt, Western China. *Environ. Earth Sci.* 76 (1), 31–15. doi:10.1007/s12665-016-6342-6

The Geothermal Geological Team of Tibet (1990). *Exploration report for the Yangyi geothermal field of the Tibet autonomous region*.

Tian, J., Pang, Z. H., Guo, Q., Wang, Y. C., Li, J., Huang, T. M., et al. (2018). Geochemistry of geothermal fluids with implications on the sources of water and heat recharge to the Rekeng high-temperature geothermal system in the Eastern Himalayan Syntax. *Geothermics* 74, 92–105. doi:10.1016/j.geothermics.2018.02.006

Tian, J., Pang, Z. H., Wang, Y. C., and Guo, Q. (2019). Fluid geochemistry of the Cuopu high temperature geothermal system in the eastern Himalayan syntaxis with implication on its Genesis. *Appl. Geochem.* 110, 104422. doi:10.1016/j.apgeochem.2019.104422

Tian, Z., Yang, Z. Q., Bendick, R., Zhao, J. L., Wang, S. D., Wu, X. L., et al. (2019). Present day distribution of deformation around the southern Tibetan plateau revealed by geodetic and seismic observations. *J. Asian earth Sci.* 171, 321–333. doi:10.1016/j.jseaes.2018.12.018

Vakulchuk, R., Overland, I., and Scholten, D. (2020). Renewable energy and geopolitics: A review. *Renew. Sustain. Energy Rev.* 122, 109547. doi:10.1016/j.rser.2019.109547

Wang, J. Y. "Discussions on geothermal energy exploration and utilization of China, from the point of world geothermal energy," in Proceedings of the Workshop on Chinese Geothermal Energy Exploration Scientifically, Beijing, China, 2009 (Beijing: Geology Press), 3–6.

Wang, P., Chen, X. H., Shen, L. C., Wu, K. Y., Huang, M. Z., and Xiao, Q. (2016). Geochemical features of the geothermal fluids from the Mapamyum non volcanic geothermal system (Western Tibet, China). *J. Volcanol. Geotherm. Res.* 320, 29–39. doi:10.1016/j.jvolgeores.2016.04.002

Wang, X. M., Cui, J. Y., Liu, Y. A., and Pei, L. Y. (2014). Discussion of correction method for mass fractionation effect of strontium spike isotopic ratios. *World Nucl. Geosci.* 31 (1), 48–52. doi:10.2343/geochemj.2.0448

Wang, X., and Tang, Z. (2020). The first large scale bioavailable Sr isotope map of China and its implication for provenance studies. *Earth. Sci. Rev.* 210, 103353. doi:10.1016/j.earscirev.2020.103353

Wang, Y. (2021). PhD dissertation. Yunnan, China: Institute of Geophysics China Earthquake Administration, P152.A research on geochemical characteristics of geothermal fluids in southeast yunnan province.

Wright, T. J., Parsons, B., England, P. C., and Fielding, E. J. (2004). InSAR observations of low slip rates on the major faults of Western Tibet. *Science* 305, 236–239. doi:10.1126/science.1096388

Wu, K. Y., Shen, L. C., Wang, X. G., Xiao, Q., and Wang, P. (2011). Study on hydrochemical features of hot springs in Langjiu geothermal field, Tibet, China. *Carsologica Sin.* 30 (1), 1–8.

Xu, Z. F., and Liu, C. Q. (2010). Water geochemistry of the Xijiang basin rivers, South China: Chemical weathering and CO_2 consumption. *Appl. Geochem.* 25, 1603–1614. doi:10.1016/j.apgeochem.2010.08.012

Yan, J. J. (2019). *Geochronology, Geochemistry and petrogenesis of mesozoic magmatic rocks in Shiquanhe area, Tibetan plateau* (Beijing, China: China University of Geosciences), 1–160.

Yan, Y., Zhou, X. C., Liao, L. X., Tian, J., Li, Y., Shi, Z. M., et al. (2022). *Hydrogeochemical characteristic of geothermal water and precursory anomalies along the Xianshuihe fault zone, Southwestern China. water* 14, 550.

Yao, T. D., Masson Delmotte, V., Gao, J., Yu, W. S., Yang, X. X., Risi, C., et al. (2013). A review of climatic controls on $\delta^{18}O$ in precipitation over the Tibetan Plateau: Observations and simulations. *Rev. Geophys.* 51 (4), 525–548. doi:10.1002/rog.20023

Yu, J., Zhang, H., Yu, F., and Liu, D. (1984). Oxygen and hydrogen isotopic compositions of meteoric waters in the eastern part of Xizang. *Geochemistry* 3 (2), 93–101. doi:10.1007/bf03179285

Yuan, J., Guo, Q., and Wang, Y. (2014). Geochemical behaviors of boron and its isotopes in aqueous environment of the Yangbajing and Yangyi geothermal fields, Tibet, China. *J. Geochem. Explor.* 140, 11–22. doi:10.1016/j.gexplo.2014.01.006

Zainal, S., Ismail, M. A. M., Mostafa, R., Narita, N., Mahmood, N., and Ng, S. M. (2016). Hydrogeochemistry of tunnel seepage water along the contact of zone of metasedimentary and granitic rock within the Pahang Selangor Raw Water Transfer Tunnel Project. *Arabian J. Geosciences* 9 (4), 1–11. doi:10.1007/s12517-015-2260-

Zhang, C. S., Zhang, Y. C., and Wu, M. L. (2003). Study on relationship between earthquake and hydro geochemistry of groundwater in southern part of North South Earthquake Belt in China. *J. Geomechanics* 9 (3), 21–30. (in Chinese with English abstract).

Zhao, C. P., Chen, Y. L., Wang, Y., and Zhou, Z. (2014). Geothermal field in the uppermost crust in the Ning'er Tongguan volcanic zone, Southwest China: Implications for tectonics and magmatism. *Acta Petrol. Sin.* 30 (12), 3645–3656. (in Chinese with English abstract).

Zhao, J., Yuan, X., Liu, H., Kumar, P., Pei, S., Kind, R., et al. (2010). The boundary between the Indian and Asian tectonic plates below Tibet. *Proc. Natl. Acad. Sci. U. S. A.* 107, 11229–11233. doi:10.1073/pnas.1001921107

Zhu, C. Y., Wang, G. C., Leloup, P. H., Cao, K., Mahéo, G., Chen, Y., et al. (2021). Role of the early Miocene jinhe-qinghe thrust belt in the building of the southeastern Tibetan plateau topography. *Tectonophysics* 811, 228871. doi:10.1016/j.tecto.2021.228871

Zuurdeeg, B. W., and Van der Weiden, M. J. J. (1985). "Geochemical aspects of European bottled waters, geochemical aspects of European bottled waters," in *Geothermics, thermal-mineral waters and hydrogeology*. Greece: Theophrastus, 235–264.